

Gate-tunable spin Hall effect in an all-light-element heterostructure: graphene with copper oxide

Haozhe Yang¹, Maider Ormaza², Zhendong Chi¹, Eoin Dolan¹, Josep Inglá-Aynés¹, C.K. Safeer¹, Franz Herling¹, Nerea Ontoso¹, Marco Gobbi^{1,3,4}, Beatriz Martín-García^{1,3}, Frederik Schiller^{4,5}, Luis E. Hueso^{1,3}, Fèlix Casanova^{1,3}*

¹ CIC nanoGUNE BRTA, 20018 Donostia-San Sebastian, Basque Country, Spain.

² Departamento de Polímeros y Materiales Avanzados: Física Química y Tecnología Facultad de Químicas, UPV/EHU, 20080 Donostia-San Sebastián, Basque Country, Spain

³ IKERBASQUE, Basque Foundation for Science, 48009 Bilbao, Basque Country, Spain.

⁴ Centro de Física de Materiales (CSIC-EHU/UPV) and Materials Physics Center (MPC), 20018 Donostia-San Sebastian, Basque Country, Spain.

⁵ Donostia International Physics Center, 20018 Donostia-San Sebastian, Basque Country, Spain

KEYWORDS: Spin Hall effect, Graphene, Spin-to-charge conversion, Light metal oxide

ABSTRACT

Graphene is a light material for long-distance spin transport due to its low spin-orbit coupling, which at the same time is the main drawback to exhibit a sizeable spin Hall effect. Decoration by light atoms has been predicted to enhance the spin Hall angle in graphene while retaining a long spin diffusion length. Here, we combine a light metal oxide (oxidized Cu) with graphene to induce the spin Hall effect. Its efficiency, given by the product of the spin Hall angle and the spin diffusion length, can be tuned with the Fermi level position, exhibiting a maximum (1.8 ± 0.6 nm at 100 K) around the charge neutrality point. This all-light-element heterostructure shows a larger efficiency than conventional spin Hall materials. The gate-tunable spin Hall effect is observed up to room temperature. Our experimental demonstration provides an efficient spin-to-charge conversion system free from heavy metals and compatible with large-scale fabrication.

Generation, manipulation, and transport of spin currents is a longstanding topic of interest in spintronics^{1–3}. A very convenient way to create (and detect) such spin currents is by exploiting spin-charge interconversion phenomena, such as the spin Hall effect (SHE)⁴ or the Edelstein effect (EE)^{5,6} and their reciprocal effects. They usually require spin-orbit coupling (SOC)^{4–6}, a relativistic effect which arises from the effective magnetic field felt by the electron in its rest frame, due to the electrostatic potential of the positive nucleus. SOC increases with the atomic number Z (with a Z^4 dependence based on the hydrogen atom model approximation⁷). Most materials investigated for spin-charge interconversion contain high-Z elements such as heavy metals⁴ or topological insulators⁸, although low-Z elements have recently drawn attention for the potential use of their orbital angular momentum^{9,10}. Additionally, the recent focus on the large spin momentum-locking in heterostructures and interfaces^{11,12} indicates the critical role of the interfacial effect in condensed matter systems^{7,13–15}.

Van der Waals materials, which can be exfoliated down to the single atomic thickness and can be combined by stacking them into heterostructures¹⁶, provide a platform for investigating spin-charge interconversion from both basic and applied perspectives^{17,18}. As the prototypical van der

Waals material, graphene exhibits high mobility, gate tunability, and a long spin lifetime¹⁹, being thus considered one of the best materials for spin transport²⁰. However, the low intrinsic SOC makes pristine graphene unsuitable for spin-charge interconversion. One solution is to induce SOC in graphene by proximity with a transition-metal dichalcogenide (TMD), a system which was predicted to show SHE^{21–24} and EE^{23–25}, and was later confirmed experimentally^{26–29}. TMD-proximitized graphene shows a sizeable spin Hall angle (θ_{SH}) while preserving a long spin diffusion length (λ_s)^{26–28}. This unique combination provides a large spin-to-charge conversion length ($\theta_{SH}\lambda_s$), which is considered an essential figure of merit for spin-orbit-based devices³⁰, such as the magnetoelectric spin-orbit (MESO) logic³¹. However, scaling up TMD/graphene van der Waals heterostructures for integrated devices is still challenging^{32–34}, as the deterministic mechanical transfer technique required to keep a clean interface^{35,36} limits the number of devices per chip.

An alternative route to enhance SOC in graphene is to decorate it with adatoms^{37–41}, which is possible to integrate into a large-scale fabrication process. High-Z atoms can induce SOC in graphene^{37–39}, and have been observed to exhibit SHE⁴². Low-Z atoms, however, are also predicted to induce SOC in graphene^{40,41}. One representative element is copper (Cu): a low-cost light metal which has also been widely used as the catalytic substrate for large-scale CVD graphene growth^{43,44}. Cu shows a weaker SOC compared with high-Z elements, although recent studies unveiled that charge-to-spin conversion in Cu can be enhanced with ambient oxidation^{45–47}. Furthermore, theoretical works have demonstrated that Cu can induce SOC both intrinsically by proximity effect⁴¹ and extrinsically by adatom decoration⁴⁰. This extrinsic mechanism has been predicted to induce SHE by skew scattering^{48,49}, with tunable θ_{SH} by changing the Fermi level position due to the preservation of the 2D Dirac cone (linear dispersion in the band structure). Even though the observation of SHE in graphene decorated with metallic adatoms has been reported using a non-local Hall bar⁵⁰, such configuration is prone to spurious effects^{49,51–54} and an unambiguous demonstration using spin precession with polarization-selective electrodes is lacking.

In this letter, we report the first experimental observation of the SHE and its inverse in a graphene/oxidized copper (CuO_x) heterostructure by measuring spin precession in a lateral spin valve. The Cu layer is grown on the graphene layer without damaging its crystal structure. Moreover, the charge-to-spin conversion output voltage can be tuned by electrical gating. By analyzing our results, we confirm that θ_{SH} and $\theta_{SH}\lambda_s$ are also gate tunable, showing a maximum value around the charge neutrality point (CNP) of graphene, in agreement with the theoretical predictions^{48,49}. Moreover, the gate-tunable SHE can be observed up to room temperature, making this system an ideal candidate for large scale fabrication.

The SHE present at a CuO_x /graphene heterostructure is illustrated in Figure 1(a). Because of the 2D nature of graphene, by applying an in-plane current (I_c) along y , the SHE generates a transverse in-plane spin current (I_s) along x with out-of-plane spin polarization. I_s propagates through the adjacent pristine graphene arm and can be non-locally detected by a ferromagnetic (FM) electrode. The reciprocal effect, inverse spin Hall effect (ISHE), converts I_s into a transverse I_c . We thus designed and fabricated a device that can detect the spin-to-charge and charge-to-spin conversion by combining a graphene Hall bar (with CuO_x on top of the cross-junction, and arms of pristine graphene) with a FM electrode (see Figure 1b). Adjacent pairs of FM electrodes are used to

calibrate the spin injection efficiency of the FM contacts and the spin transport properties of the pristine graphene, required to quantify θ_{SH} . Details of the device fabrication are given in Supporting Information Note 1.

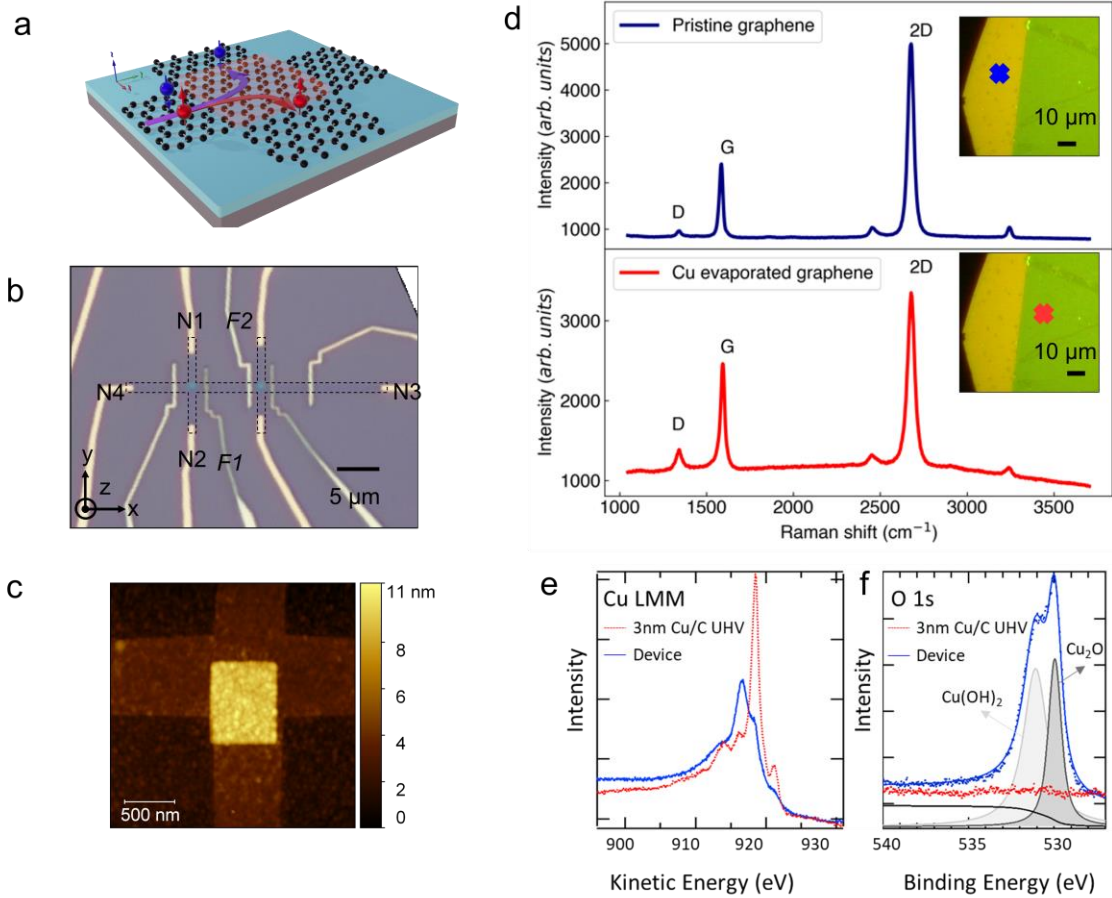


Figure 1. (a) Sketch of the spin Hall effect expected in CuO_x-covered graphene: the spin current is generated transverse to the charge current direction, with out-of-plane spin polarization. (b) Optical image of Sample 1. The dashed lines follow the edges of the graphene channel. The non-magnetic contact (N1 to N4) and magnetic electrodes (F1 and F2) are indicated. (c) AFM image of the heterostructure at the graphene Hall cross-junction shows a continuous topography of the CuO_x layer. (d) Raman spectra for pristine graphene (upper panel) and the same graphene covered with evaporated CuO_x (lower panel) indicate no clear damage induced by the evaporation. The insets show the optical image of the pristine graphene region (yellow) and the region covered by CuO_x (green), with an indication of the Raman laser spot position. (e) Cu LMM Auger spectra and (f) O 1s spectra for a 3-nm-thick Cu film grown on top of graphite under UHV conditions (in red) and for a 5-nm-thick Cu film grown on graphite and left in air for 72 h prior to measurement, following the same protocol as the device fabrication (in blue). Fitting of the latter shows two main contributions, one from Cu₂O and another one from Cu(OH)₂.

Cu has low affinity to carbon (C) and does not form any carbide phases^{55,56}. It is considered to form only soft bonds with C via charge transfer from the π electrons in the sp^2 hybridized C to the empty 4s states of Cu⁴⁴. Before measuring the devices, we performed several characterizations. We first checked whether graphene is degraded after thermally evaporating Cu on top and leaving it to oxidize. The control experiment was performed on a CVD-grown single layer graphene, in which a selected area is covered by 5 nm of thermally evaporated Cu, followed by ambient oxidization. The Raman spectra of the evaporated/non-evaporated areas are plotted in Figure 1(d),

both showing well-defined 2D and G peaks, indicating no structural damage⁵⁷ of graphene when forming the heterostructure. To characterize the electrical properties of CuO_x, we fabricated a double Hall bar with 5-nm-thick Cu grown and oxidized in the same conditions and measured its charge transport properties, indicating that the conductivity of CuO_x is at least seven orders of magnitude smaller than that of graphene (see Supporting Information Figure S7). This confirms that all charge transport (and thus spin transport) in our devices only occurs in graphene. The atomic force microscopy (AFM) image in Figure 1(c) shows the topography of the heterostructure, exhibiting a continuous CuO_x film with root mean square roughness of 0.6 nm, much smaller than the thickness.

X-ray photoelectron spectroscopy (XPS) was employed to unveil the chemical state of Cu on the graphene surface. Figure 1(e) shows the comparison between the Cu-LMM Auger transition of a 3-nm-thick Cu grown on graphite in ultra-high vacuum (UHV) and a 5-nm-thick Cu film grown on graphite after 72 h of air exposure. The former shows metallic state, while the latter, which is analogous to the one employed to fabricate the devices, shows a complete oxidation⁵⁸. Furthermore, the O 1s spectrum of the 5-nm-thick film in Figure 1(f) shows two main contributions, one related to Cu₂O and another to Cu(OH)₂, with binding energies 530.0 eV and 531.1 eV, respectively, whereas the O 1s peak vanishes for the 3-nm-thick Cu grown in UHV. No traces of C-O or Cu-C bonds have been found on the C 1s spectrum, as shown in Supporting Information Note 3. Additional XPS measurements have been carefully performed to further investigate the oxidation process of the Cu on the surface. From this analysis, we conclude that the amount of metallic Cu on the graphene surface is negligible.

After confirming that graphene is not structurally damaged, Cu is fully oxidized and that CuO_x and Cu(OH)₂ are not conductive and fully cover graphene, we proceed to study the spin transport properties of our devices. First, we use two FM electrodes as the spin injector (F1) and detector (F2) to extract the spin transport properties of the pristine graphene (see Figure 2(a)). A charge current I_c is applied from F1 to N4, and a non-local voltage V_{NL} is measured between F2 and N3. We normalized V_{NL} by I_c to obtain a non-local resistance R_{NL} . The relative alignment of the magnetization of F1 and F2 electrodes (parallel or antiparallel) can be set with an external magnetic field (B_y) applied along their easy axis y , because the different widths of F1 and F2 yield different coercivities. A magnetic field (B_x) along the in-plane hard axis x of the FM contacts is swept from zero until full saturation of the FM electrodes. At lower fields, spins in graphene precess in the y - z plane and R_{NL} exhibits a symmetric Hanle precession behavior. One representative result measured at 100 K with a back gate voltage (V_g) of 30 V is shown in Figure 2(b). The pure spin precession signal ΔR_{NL} plotted in Figure 2(c) is obtained by subtracting the R_{NL} curves between the parallel (R_{NL}^P) and antiparallel (R_{NL}^{AP}) configuration.

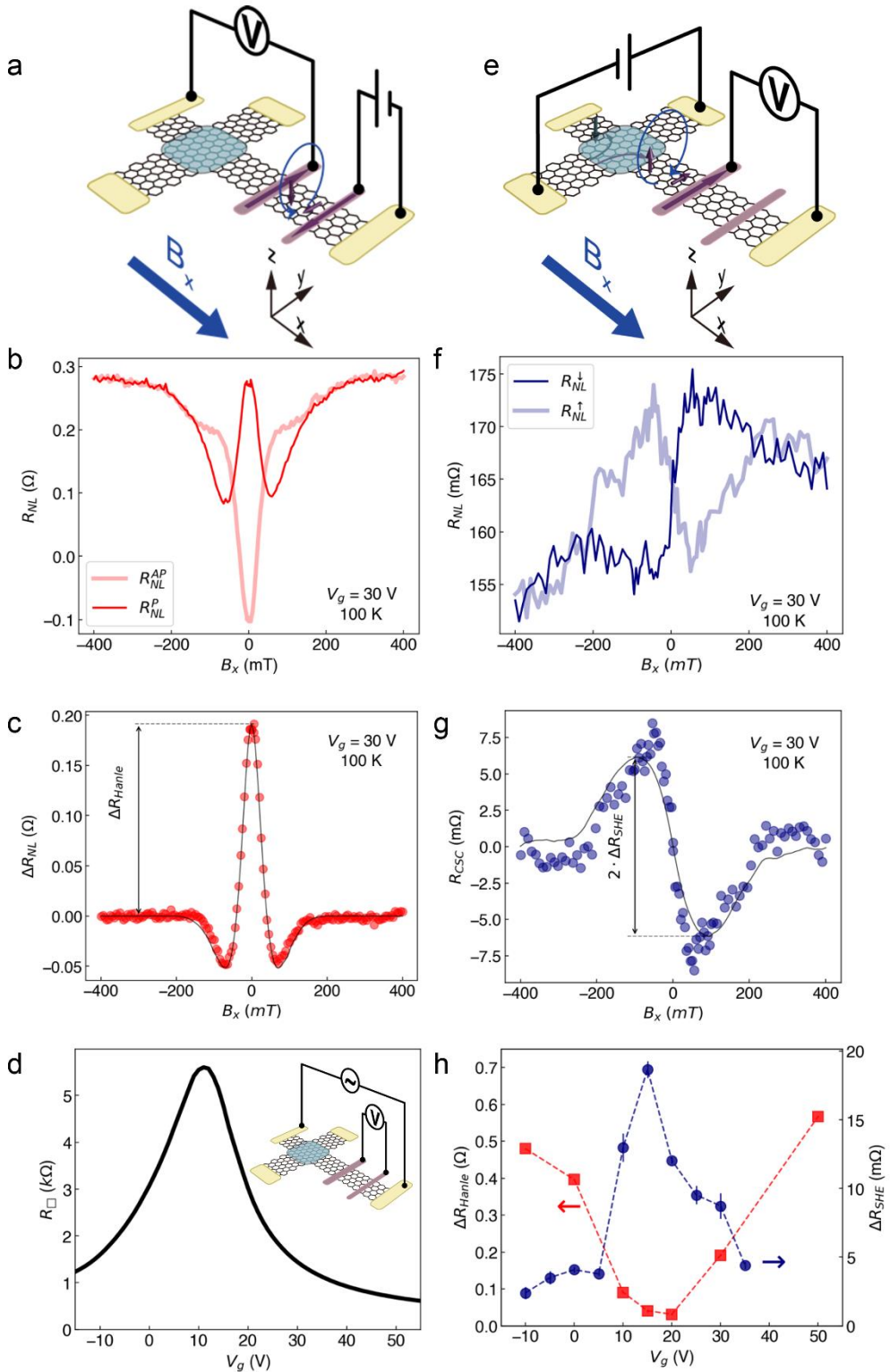


Figure 2. (a) Measurement configuration for symmetric Hanle precession with standard electrical spin injection and detection using two FM electrodes. An in-plane magnetic field, B_x , is applied to induce precession of the y -polarized spins injected from the FM electrode into the graphene. (b) Non-local resistance as a function of B_x measured at 100

K and $V_g = 30$ V using the configuration in (a), with F1 and F2 electrodes set in a parallel (R_{NL}^P , dark-red line) and antiparallel (R_{NL}^P , light-red line) configuration. (c) Net symmetric Hanle precession signal extracted from the two curves in (b) by taking $\Delta R_{NL} = (R_{NL}^P - R_{NL}^{AP})/2$. The gray solid line is a fit of the data to the solution of the Bloch equation. The amplitude of the signal, ΔR_{Hanle} , is labeled. (d) Square resistance, R_{\square} , of the pristine graphene as a function of V_g measured at 100 K using the four-point configuration illustrated in the inset. (e) Measurement configuration for antisymmetric Hanle precession with charge-to-spin conversion at the CuO_x -covered graphene and detection using a FM electrode. B_x is applied to induce precession of the z -polarized spins, originating from the SHE in decorated graphene. (f) Non-local resistance as a function of B_x measured at 100 K and $V_g = 30$ V using the configuration in (e), with initial positive (R_{NL}^{\uparrow} , light-blue line) and negative (R_{NL}^{\downarrow} , dark-blue line) magnetization direction of F1. (g) Net antisymmetric Hanle precession signal extracted from the two curves in (f) by taking $R_{CSC} = (R_{NL}^{\uparrow} - R_{NL}^{\downarrow})/2$ and antisymmetrizing it. The gray solid line is a fit of the data to the solution of the Bloch equation. The amplitude of the signal, ΔR_{SHE} , is labeled. (h) Amplitude of the symmetric (ΔR_{Hanle} , blue squares) and antisymmetric (ΔR_{SHE} , red circles) Hanle precession signals at 100 K plotted as a function of V_g . All data corresponds to Sample 1.

After confirming the spin transport in our device, we perform the charge-to-spin conversion measurements (see Figure 2(e)). I_c is applied along the transverse channel y from N1 to N2. At the CuO_x /graphene heterostructure, the SHE generates an I_s along x with an out-of-plane spin polarization, which diffuses into the pristine graphene channel. By applying B_x , the out-of-plane spins precess in the y - z plane. Due to this precession, the diffusing spins develop a y component which can then be detected by F1, which is magnetized along y , as a non-local voltage (again normalized into a non-local resistance, $R_{NL}^{\uparrow} = V_{NL}/I_c$). This process results in an antisymmetric spin precession curve with a maximum and a minimum at a certain $\pm B_x$ value. When reversing the magnetization of F1, the antisymmetric Hanle curve R_{NL}^{\downarrow} is reversed because the detector senses the opposite y -spin component. To obtain the two curves, we initialize the F1 magnetization with a B_y field, then sweep B_x from zero until saturation of the electrode. This operation is repeated for the two polarizations and B_x polarities. One representative charge-to-spin conversion curve set measured at 100 K and $V_g = 30$ V is shown in Figure 2(f), exhibiting the expected behavior. The pure charge-to-spin precession signal ΔR_{CSC} with out-of-plane spin polarization (due to the SHE), plotted in Figure 2(g), has been obtained as follows: (1) subtracting the R_{NL} curves between the positive (R_{NL}^{\uparrow}) and negative (R_{NL}^{\downarrow}) alignment of the F1 magnetization, followed by (2) an antisymmetrization of the obtained curve with respect to the magnetic field. The first step removes any initial-magnetization independent components, such as local magnetoresistance, ordinary Hall effect⁵⁹ and conventional EE^{26,60}. The second step eliminates the possible contribution of unconventional charge-to-spin conversion with spins polarized along y , which has been observed in some van der Waals heterostructures^{60–63}. The reciprocal experiment (inverse SHE) is shown in Supporting Information Figure S11 and confirms that we are in the linear response regime. A control experiment in a reference device without CuO_x as an adlayer exhibits no spin-to-charge signal (see Supporting Information Figure S10).

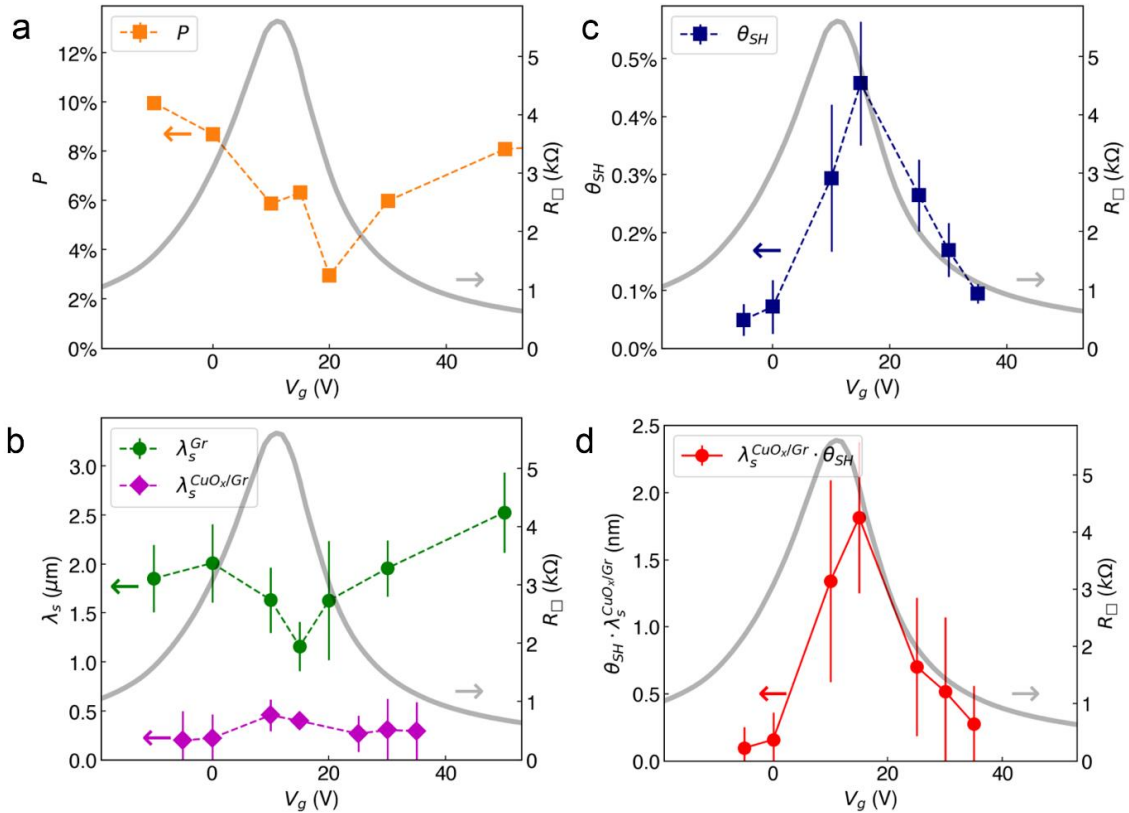


Figure 3. Gate voltage dependence of (a) spin polarization of Co/TiO_x electrode, (b) spin diffusion length of pristine graphene (green circles) and CuO_x/graphene (magenta diamonds), (c) spin Hall angle of CuO_x/graphene, and (d) spin-to-charge conversion length of CuO_x/graphene. All results are taken from Sample 1 at 100 K. The square resistance is plotted in all panels as a solid gray line for comparison.

Next, we studied how the charge-to-spin conversion is tuned with V_g . We first measured the charge transport properties with a four-point configuration. The gate-dependent square resistance (R_{\square}) of pristine graphene measured at 100 K is plotted in Figure 2(d), showing a representative Dirac material feature, with the resistance maximum corresponding to the CNP. The CuO_x-covered graphene and the pristine graphene exhibit a similar doping, as shown in Supporting Information Figure S12. ARPES experiments have shown that graphene preserves its Dirac cone in contact with copper oxide⁶⁴, which is promising for gate-tunable electronics. Then, we measured the symmetric and antisymmetric Hanle precession curves at different V_g , taking the gate-dependent spin injection efficiency and spin transport properties of the pristine graphene⁶⁵. The amplitude ΔR_{Hanle} of the symmetric Hanle curve (defined in Figure 2(c)) and the amplitude ΔR_{SHE} of the antisymmetric Hanle curve (defined in Figure 2(g)) are plotted in Figure 2(h). Here ΔR_{Hanle} and ΔR_{SHE} exhibit the opposite behavior with V_g . ΔR_{Hanle} shows a minimum around the CNP, increasing when the carrier density is higher. Such decrease of the spin signal around the CNP is expected when the FM/graphene contacts have a low contact resistance (R_c) due to the spin conductivity mismatch⁶⁶, which is our case ($R_c=1.7$ k Ω and 3 k Ω estimated from a three-point measurement). In stark contrast, ΔR_{SHE} shows the highest value around the CNP, where the spin injection efficiency is lowest, implying that the charge-to-spin conversion efficiency should be larger around the CNP to achieve an overall larger output signal.

For a quantitative analysis of the spin transport and the charge-to-spin conversion efficiency, both the symmetric and antisymmetric Hanle precession data are fitted to the numerical solution of the Bloch equation (see solid gray lines in Figs. 2(c) and 2(g)). The fitting procedure is detailed in Supporting Information Note 2. From the fit of the symmetric Hanle curve, we obtain the spin polarization P of the FM contact and the spin lifetime, τ_s^{gr} , of the pristine graphene. In order to decrease the number of fitting parameters, we assume the spin and charge diffusion constants to be equal ($D_s = D_c$)⁶⁶ and extract D_c from R_{\square} . The gate dependence of P is plotted in Figure 3(a), with values ranging from $9.9 \pm 0.1\%$ at $V_g = -10$ V down to $3.0 \pm 0.2\%$ at $V_g = 20$ V, close to the CNP. The spin diffusion length $\lambda_s^{gr} = \sqrt{\tau_s^{gr} D_s}$ of the pristine graphene is plotted in Figure 3(b), with values ranging from 2.5 ± 0.4 μm at $V_g = 50$ V to a minimum value of 1.2 ± 0.2 μm at $V_g = 15$ V, close to the CNP.

From the fit of the antisymmetric Hanle curve, and by fixing P and τ_s^{gr} obtained from the previous fit, we obtain the spin Hall angle θ_{SH} and the spin lifetime $\tau_s^{CuOx/gr}$ of the decorated graphene. Note that no evidential spin lifetime anisotropy of the functionalized graphene was observed, shown in Supporting Information Figure S14. The gate dependence of θ_{SH} is plotted in Figure 3(c), showing a peak of $0.5 \pm 0.1\%$ around the CNP and decreasing away from the CNP. Resonant skew scattering has been theoretically predicted in atomic-decorated graphene, exhibiting a spin Hall angle which is tuned with the Fermi level position and the largest value expected near the CNP^{48,49}, in excellent agreement with our observation. This extrinsic mechanism is therefore the most likely scenario in our system.

Note that the obtained value of θ_{SH} is even larger than that of $\text{BiO}_x/\text{graphene}$ at the same temperature ($\sim 0.25\%$ at 100 K), although Bi has a much larger Z , and thus SOC, than Cu. The low affinity and ability to form soft bonds with carbon⁴⁴, discussed previously, makes Cu not only an excellent catalyst for graphitic carbon formation but could also induce SOC by proximity. Considering the well-preserved crystal structure of graphene shown by Raman spectroscopy in Figure 1(d) and the continuous topography of the CuO_x layer grown on graphene shown in the AFM image in Figure 1(c), a long-range flat interface is possible to be formed, which is an ideal proximitized system. In this case, we cannot rule out that a spin-orbit proximity effect such as the one calculated in Ref. ⁴¹ is able to provide an extra contribution to our large θ_{SH} in the CuO_x -covered graphene.

The spin diffusion length of the $\text{CuO}_x/\text{graphene}$ heterostructure is calculated as $\lambda_s^{CuOx/gr} = \sqrt{\tau_s^{CuOx/gr} D_s}$ and is plotted in Figure 3(c). $\lambda_s^{CuOx/gr}$ is substantially shorter (ranging between 450 ± 160 nm at $V_g = 10$ V and 190 ± 300 nm at $V_g = -5$ V) than λ_s^{gr} , which is expected because an enhanced SOC decreases the spin lifetime. The gate-dependent spin-to-charge conversion length ($\theta_{SH} \lambda_s^{CuOx/gr}$), plotted in Figure 3(d), also exhibits a peak around the CNP. At $V_g = 15$ V, $\theta_{SH} \lambda_s^{CuOx/gr} = 1.80 \pm 0.56$ nm, which is one order of magnitude larger than the value at $V_g = 0$ V (0.15 ± 0.20 nm). This is a remarkable result: while we have only low-Z elements in our material system (Cu, O, C), the value is higher than in conventional large SOC materials, such as heavy metals (0.2 nm for Pt⁶⁷, 0.34 nm for W⁶⁸) or metallic Rashba interfaces (0.3 nm for Ag/Bi⁶⁹, -0.17

nm for Cu/Au⁷⁰), and is of the same order of magnitude as in material systems such as topological insulators (2.1 nm for α -Sn⁷¹), oxide 2DEGs (6.4 nm for LAO/STO¹¹), or heavy metal oxide/graphene heterostructures (1 nm for BiO_x/graphene at 100 K⁴²).

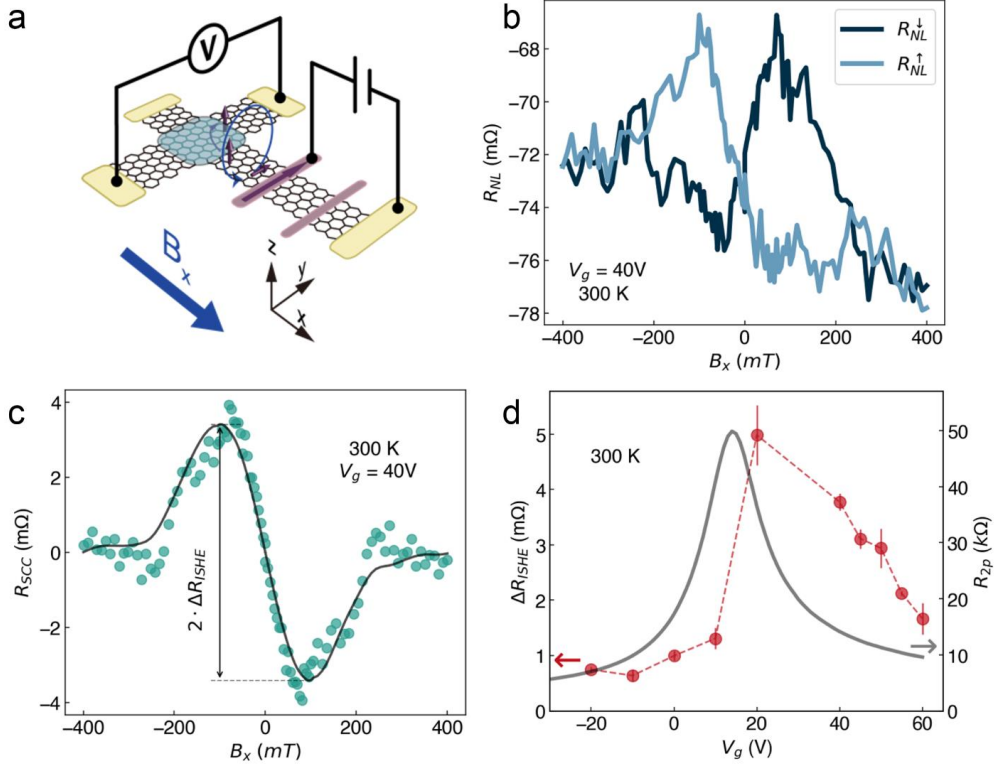


Figure 4. (a) Measurement configuration for antisymmetric Hanle precession with spin injection using a FM electrode and spin-to-charge conversion at the CuO_x-covered graphene. B_x is applied to induce precession of the y -polarized spins towards z , in order to be detected by ISHE in decorated graphene. (b) Non-local resistance as a function of B_x measured at 300 K and $V_g = 40$ V in Sample 2 using the configuration in (a) with initial positive (R_{NL}^{\uparrow} , light-blue line) and negative (R_{NL}^{\downarrow} , dark-blue line) magnetization direction of the FM injector. (c) Net antisymmetric precession signal extracted from the two curves in (b) by taking $R_{SSC} = (R_{NL}^{\uparrow} - R_{NL}^{\downarrow})/2$ and antisymmetrizing it. The gray solid line is a fit of the data to the solution of the Bloch equation. The amplitude of the signal, ΔR_{ISHE} , is labeled. (d) Gate dependence of ΔR_{ISHE} at 300 K (solid red circles). The two-point resistance as a function of V_g of the CuO_x-covered graphene at the cross-junction of the Hall bar measured at 300 K is also plotted (solid gray line).

Finally, we studied the spin-to-charge conversion of CuO_x/graphene heterostructure at room temperature (see Figure 4(a)). The non-local spin precession measurement measured at 300 K and $V_g = 40$ V in Sample 2 is exemplary shown in Figure 4(b). Sample 2 is fabricated on the same single layer graphene flake as Sample 1, with the details shown in Supporting Information Figure S9. The pure spin-to-charge precession signal R_{SSC} due to the ISHE, obtained in the same way as for R_{CSC} , is plotted in Figure 4(c) and shows a clear antisymmetric Hanle behavior. We also observed that its amplitude ΔR_{ISHE} could be tuned with V_g , exhibiting the largest output at 20 V, as shown by solid red circles in Figure 4(d). The solid gray line in Figure 4(d) is the two-point resistance measurement of the transverse Hall arm at room temperature, indicating the CNP to be around 15 V, close to the ΔR_{ISHE} maximum. An estimation of θ_{SH} and $\lambda_s^{CuOx/gr}$ at room temperature requires knowing P and λ_s^{gr} at this temperature. However, the shorter λ_s^{gr} at 300 K decreases the signal for the symmetric Hanle precession, yielding a low signal-to-noise ratio that

leads to an unreliable estimation of the spin transport parameters. We therefore use P and λ_s^{gr} values obtained at 100 K for Sample 1 to estimate θ_{SH} and $\lambda_s^{CuOx/gr}$ at room temperature. With this approximation, we would obtain $\theta_{SH} = 0.34 \pm 0.18\%$ and $\lambda_s^{CuOx/gr} = 370 \pm 430$ nm at room temperature and $V_g = 20$ V, corresponding to a $\theta_{SH}\lambda_s^{CuOx/gr}$ of 1.2 ± 1.6 nm. The robustness of this effect is further confirmed by additional samples (including trilayer graphene) shown in Supporting Information Figure S13.

In conclusion, we report the first unambiguous experimental observation of the SHE in graphene induced by a light-metal oxide. The CuO_x-covered graphene keeps its structural and electrical properties, while acquiring SOC from the oxidized Cu adlayer that leads to SHE up to room temperature. After a careful estimation considering the gate-dependent spin transport properties of the pristine graphene and the FM contacts, we find that the spin Hall angle and the spin-to-charge conversion length of CuO_x/graphene are gate tunable, with maximum values around the CNP. These values are comparable to those observed in heavy metal oxide/graphene heterostructures. Cu being a well-established light element for the graphene industry, CuO_x/graphene heterostructures could be an ideal candidate for large-scale spintronic applications.

ASSOCIATED CONTENT

Supporting Information.

Additional details on methods, spin precession fitting process, XPS analysis, electrical characterization of oxidized copper, optical image of devices during the fabrication process, optical and SEM images of Sample 2, reference non-local Hall bar without CuO_x, reciprocity between spin Hall effect and inverse spin Hall effect, charge transport properties of the pristine graphene and the CuO_x-covered graphene, reproducibility.

AUTHOR INFORMATION

Corresponding Author

*E-mail: f.casanova@nanogune.eu

Author Contributions

H.Y. and F.C. conceived the study. H.Y. performed the sample fabrication, electrical, and optical measurements, with the help of Z.C., E.D., J.I.A, C.K.S., F.H., N.O. and B. M.-G.. M.O. and F.S. performed the XPS experiments. All authors contributed to the discussion of the results and their interpretation. H.Y. and F.C. wrote the manuscript with input from all authors.

ACKNOWLEDGMENTS

We acknowledge funding by the “Valleytronics” Intel Science Technology Center, by the Spanish MICINN (Project No. PID2021-122511OB-I00 and “Maria de Maeztu” Units of Excellence Programme No. CEX2020-001038-M), by the European Union H2020 under the Marie Skłodowska-Curie Actions (Project Nos. 0766025-QuESTech and 955671-SPEAR) and by Diputación de Gipuzkoa (Project No. 2021-CIEN-000037-01). Z.C. acknowledges postdoctoral fellowship support from “Juan de la Cierva” Programme by the Spanish MICINN (grant No. FJC2021-047257-I).

REFERENCES

- (1) Žutić, I.; Fabian, J.; Sarma, S. Das. Spintronics: Fundamentals and Applications. *Rev. Mod. Phys.* **2004**, *76* (2), 323–410.

(2) Maekawa, S.; Valenzuela, S. O.; Saitoh, E.; Kimura, T. *Spin Current*; Oxford University Press, 2017; Vol. 22.

(3) Manchon, A.; Železný, J.; Miron, I. M.; Jungwirth, T.; Sinova, J.; Thiaville, A.; Garello, K.; Gambardella, P. Current-Induced Spin-Orbit Torques in Ferromagnetic and Antiferromagnetic Systems. *Rev. Mod. Phys.* **2019**, *91* (3), 035004.

(4) Sinova, J.; Valenzuela, S. O.; Wunderlich, J.; Back, C. H.; Jungwirth, T. Spin Hall Effects. *Rev. Mod. Phys.* **2015**, *87* (4), 1213–1260.

(5) Bihlmayer, G.; Noël, P.; Vyalikh, D. V.; Chulkov, E. V.; Manchon, A. Rashba-like Physics in Condensed Matter. *Nat. Rev. Phys.* **2022**, *4* (10), 642–659.

(6) Manchon, A.; Koo, H. C.; Nitta, J.; Frolov, S. M.; Duine, R. A. New Perspectives for Rashba Spin-Orbit Coupling. *Nat. Mater.* **2015**, *14* (9), 871–882.

(7) Hellman, F.; Division, M. S.; Berkeley, L.; Hoffmann, A.; Beach, G. S. D.; Fullerton, E. E.; Macdonald, A. H.; Ralph, D. C. Interface-Induced Phenomena in Magnetism. *Rev. Mod. Phys.* **2017**, *89* (June), 025006.

(8) He, Q. L.; Hughes, T. L.; Armitage, N. P.; Tokura, Y.; Wang, K. L. Topological Spintronics and Magnetoelectronics. *Nat. Mater.* **2022**, *21* (1), 15–23.

(9) Jo, D.; Go, D.; Lee, H.-W. Gigantic Intrinsic Orbital Hall Effects in Weakly Spin-Orbit Coupled Metals. *Phys. Rev. B* **2018**, *98* (21), 214405.

(10) Sala, G.; Gambardella, P. Giant Orbital Hall Effect and Orbital-to-Spin Conversion in 3d, 5d, and 4f Metallic Heterostructures. *Phys. Rev. Res.* **2022**, *4* (3), 033037.

(11) Lesne, E.; Fu, Y.; Oyarzun, S.; Rojas-Sánchez, J. C.; Vaz, D. C.; Naganuma, H.; Sicoli, G.; Attané, J.-P.; Jamet, M.; Jacquet, E.; George, J.-M.; Barthélémy, A.; Jaffrès, H.; Fert, A.; Bibes, M.; Vila, L. Highly Efficient and Tunable Spin-to-Charge Conversion through Rashba Coupling at Oxide Interfaces. *Nat. Mater.* **2016**, *15* (12), 1261–1266.

(12) Vaz, D. C.; Trier, F.; Dyrdał, A.; Johansson, A.; Garcia, K.; Barthélémy, A.; Mertig, I.; Barnaś, J.; Fert, A.; Bibes, M. Determining the Rashba Parameter from the Bilinear Magnetoresistance Response in a Two-Dimensional Electron Gas. *Phys. Rev. Mater.* **2020**, *4* (7), 071001.

(13) Pesin, D.; MacDonald, A. H. Spintronics and Pseudospintrronics in Graphene and Topological Insulators. *Nat. Mater.* **2012**, *11* (5), 409–416.

(14) Dieny, B.; Prejbeanu, I. L.; Garello, K.; Gambardella, P.; Freitas, P.; Lehndorff, R.; Raberg, W.; Ebels, U.; Demokritov, S. O.; Akerman, J.; Deac, A.; Pirro, P.; Adelmann, C.; Anane, A.; Chumak, A. V.; Hirohata, A.; Mangin, S.; Valenzuela, S. O.; Onbaşlı, M. C.; d’Aquino, M.; Prenat, G.; Finocchio, G.; Lopez-Diaz, L.; Chantrell, R.; Chubykalo-Fesenko, O.; Bortolotti, P. Opportunities and Challenges for Spintronics in the Microelectronics Industry. *Nat. Electron.* **2020**, *3* (8), 446–459.

(15) Soumyanarayanan, A.; Reyren, N.; Fert, A.; Panagopoulos, C. Emergent Phenomena Induced by Spin-Orbit Coupling at Surfaces and Interfaces. *Nature* **2016**, *539* (7630), 509–517.

(16) Geim, A. K.; Grigorieva, I. V. Van Der Waals Heterostructures. *Nature* **2013**, *499* (7459), 419–425.

(17) Avsar, A.; Ochoa, H.; Guinea, F.; Özyilmaz, B.; van Wees, B. J.; Vera-Marun, I. J. Colloquium : Spintronics in Graphene and Other Two-Dimensional Materials . *Rev. Mod. Phys.* **2020**, *92* (2), 21003.

(18) Sierra, J. F.; Fabian, J.; Kawakami, R. K.; Roche, S.; Valenzuela, S. O. Van Der Waals Heterostructures for Spintronics and Opto-Spintronics. *Nat. Nanotechnol.* **2021**, *16* (8),

856–868.

(19) Tombros, N.; Jozsa, C.; Popinciuc, M.; Jonkman, H. T.; van Wees, B. J. Electronic Spin Transport and Spin Precession in Single Graphene Layers at Room Temperature. *Nature* **2007**, *448* (7153), 571–574.

(20) Han, W.; Kawakami, R. K.; Gmitra, M.; Fabian, J. Graphene Spintronics. *Nat. Nanotechnol.* **2014**, *9* (10), 794–807.

(21) Garcia, J. H.; Cummings, A. W.; Roche, S. Spin Hall Effect and Weak Antilocalization in Graphene/Transition Metal Dichalcogenide Heterostructures. *Nano Lett.* **2017**, *17* (8), 5078–5083.

(22) Milletari, M.; Offidani, M.; Ferreira, A.; Raimondi, R. Covariant Conservation Laws and the Spin Hall Effect in Dirac-Rashba Systems. *Phys. Rev. Lett.* **2017**, *119* (24), 246801.

(23) Garcia, J. H.; Vila, M.; Cummings, A. W.; Roche, S. Spin Transport in Graphene/Transition Metal Dichalcogenide Heterostructures. *Chem. Soc. Rev.* **2018**, *47* (9), 3359–3379.

(24) Lee, S.; De Sousa, D. J. P.; Kwon, Y. K.; De Juan, F.; Chi, Z.; Casanova, F.; Low, T. Charge-to-Spin Conversion in Twisted Graphene/WSe₂ Heterostructures. *Phys. Rev. B* **2022**, *106* (16), 165420.

(25) Offidani, M.; Milletari, M.; Raimondi, R.; Ferreira, A. Optimal Charge-to-Spin Conversion in Graphene on Transition-Metal Dichalcogenides. *Phys. Rev. Lett.* **2017**, *119* (19), 196801.

(26) Safeer, C. K.; Ingla-Aynés, J.; Herling, F.; Garcia, J. H.; Vila, M.; Ontoso, N.; Calvo, M. R.; Roche, S.; Hueso, L. E.; Casanova, F. Room-Temperature Spin Hall Effect in Graphene/MoS₂ van Der Waals Heterostructures. *Nano Lett.* **2019**, *19* (2), 1074–1082.

(27) Herling, F.; Safeer, C. K.; Ingla-Aynés, J.; Ontoso, N.; Hueso, L. E.; Casanova, F. Gate Tunability of Highly Efficient Spin-to-Charge Conversion by Spin Hall Effect in Graphene Proximity with WSe₂. *APL Mater.* **2020**, *8* (7), 071103.

(28) Benítez, L. A.; Torres, W. S.; Sierra, J. F.; Timmermans, M.; Garcia, J. H.; Roche, S.; Costache, M. V.; Valenzuela, S. O. Tunable Room-Temperature Spin Galvanic and Spin Hall Effects in van Der Waals Heterostructures. *Nat. Mater.* **2019**, *19* (2), 170–175.

(29) Ghiasi, T. S.; Kaverzin, A. A.; Blah, P. J.; van Wees, B. J. Charge-to-Spin Conversion by the Rashba-Edelstein Effect in Two-Dimensional van Der Waals Heterostructures up to Room Temperature. *Nano Lett.* **2019**, *19* (9), 5959–5966.

(30) Pham, V. T.; Groen, I.; Manipatruni, S.; Choi, W. Y.; Nikonorov, D. E.; Sagasta, E.; Lin, C. C.; Gosavi, T. A.; Marty, A.; Hueso, L. E.; Young, I. A.; Casanova, F. Spin–Orbit Magnetic State Readout in Scaled Ferromagnetic/Heavy Metal Nanostructures. *Nat. Electron.* **2020**, *3* (6), 309–315.

(31) Manipatruni, S.; Nikonorov, D. E.; Lin, C. C.; Gosavi, T. A.; Liu, H.; Prasad, B.; Huang, Y. L.; Bonturim, E.; Ramesh, R.; Young, I. A. Scalable Energy-Efficient Magnetoelectric Spin–Orbit Logic. *Nature* **2019**, *565* (7737), 35–42.

(32) Shim, J.; Bae, S.-H.; Kong, W.; Lee, D.; Qiao, K.; Nezich, D.; Park, Y. J.; Zhao, R.; Sundaram, S.; Li, X.; Yeon, H.; Choi, C.; Kum, H.; Yue, R.; Zhou, G.; Ou, Y.; Lee, K.; Moodera, J.; Zhao, X.; Ahn, J.-H.; Hinkle, C.; Ougazzaden, A.; Kim, J. Controlled Crack Propagation for Atomic Precision Handling of Wafer-Scale Two-Dimensional Materials. *Science (80-.)* **2018**, *362* (6415), 665–670.

(33) Aljarb, A.; Fu, J. H.; Hsu, C. C.; Chuu, C. P.; Wan, Y.; Hakami, M.; Naphade, D. R.; Yengel, E.; Lee, C. J.; Brems, S.; Chen, T. A.; Li, M. Y.; Bae, S. H.; Hsu, W. T.; Cao, Z.; Albaridy, R.; Lopatin, S.; Chang, W. H.; Anthopoulos, T. D.; Kim, J.; Li, L. J.; Tung, V. Ledge-Directed Epitaxy of Continuously Self-Aligned Single-Crystalline Nanoribbons of

Transition Metal Dichalcogenides. *Nat. Mater.* **2020**, *19* (12), 1300–1306.

(34) Kum, H.; Lee, D.; Kong, W.; Kim, H.; Park, Y.; Kim, Y.; Baek, Y.; Bae, S. H.; Lee, K.; Kim, J. Epitaxial Growth and Layer-Transfer Techniques for Heterogeneous Integration of Materials for Electronic and Photonic Devices. *Nat. Electron.* **2019**, *2* (10), 439–450.

(35) Frisenda, R.; Navarro-Moratalla, E.; Gant, P.; Pérez De Lara, D.; Jarillo-Herrero, P.; Gorbachev, R. V.; Castellanos-Gomez, A. Recent Progress in the Assembly of Nanodevices and van Der Waals Heterostructures by Deterministic Placement of 2D Materials. *Chem. Soc. Rev.* **2018**, *47* (1), 53–68.

(36) Castellanos-Gomez, A.; Buscema, M.; Molenaar, R.; Singh, V.; Janssen, L.; van der Zant, H. S. J.; Steele, G. A. Deterministic Transfer of Two-Dimensional Materials by All-Dry Viscoelastic Stamping. *2D Mater.* **2014**, *1* (1), 011002.

(37) Castro Neto, A. H.; Guinea, F. Impurity-Induced Spin-Orbit Coupling in Graphene. *Phys. Rev. Lett.* **2009**, *103* (2), 026804.

(38) Weeks, C.; Hu, J.; Alicea, J.; Franz, M.; Wu, R. Engineering a Robust Quantum Spin Hall State in Graphene via Adatom Deposition. *Phys. Rev. X* **2011**, *1* (2), 021001.

(39) Calleja, F.; Ochoa, H.; Garnica, M.; Barja, S.; Navarro, J. J.; Black, A.; Otrókov, M. M.; Chulkov, E. V.; Arnau, A.; Vázquez De Parga, A. L.; Guinea, F.; Miranda, R. Spatial Variation of a Giant Spin-Orbit Effect Induces Electron Confinement in Graphene on Pb Islands. *Nat. Phys.* **2015**, *11* (1), 43–47.

(40) Frank, T.; Irmer, S.; Gmitra, M.; Kochan, D.; Fabian, J. Copper Adatoms on Graphene: Theory of Orbital and Spin-Orbital Effects. *Phys. Rev. B* **2017**, *95* (3), 035402.

(41) Frank, T.; Gmitra, M.; Fabian, J. Theory of Electronic and Spin-Orbit Proximity Effects in Graphene on Cu(111). *Phys. Rev. B* **2016**, *93* (15), 155142.

(42) Safeer, C. K.; Inglá-Aynés, J.; Ontoso, N.; Herling, F.; Yan, W.; Hueso, L. E.; Casanova, F. Spin Hall Effect in Bilayer Graphene Combined with an Insulator up to Room Temperature. *Nano Lett.* **2020**, *20* (6), 4573–4579.

(43) Wang, Y.; Zheng, Y.; Xu, X.; Dubuisson, E.; Bao, Q.; Lu, J.; Loh, K. P. Electrochemical Delamination of CVD-Grown Graphene Film: Toward the Recyclable Use of Copper Catalyst. *ACS Nano* **2011**, *5* (12), 9927–9933.

(44) Mattevi, C.; Kim, H.; Chhowalla, M. A Review of Chemical Vapour Deposition of Graphene on Copper. *J. Mater. Chem.* **2011**, *21* (10), 3324–3334.

(45) Gao, T.; Qaiumzadeh, A.; An, H.; Musha, A.; Kageyama, Y.; Shi, J.; Ando, K. Intrinsic Spin-Orbit Torque Arising from the Berry Curvature in a Metallic-Magnet/Cu-Oxide Interface. *Phys. Rev. Lett.* **2018**, *121* (1), 17202.

(46) An, H.; Kageyama, Y.; Kanno, Y.; Enishi, N.; Ando, K. Spin-Torque Generator Engineered by Natural Oxidation of Cu. *Nat. Commun.* **2016**, *7* (1), 13069.

(47) Ding, S.; Ross, A.; Go, D.; Baldrati, L.; Ren, Z.; Freimuth, F.; Becker, S.; Kammerbauer, F.; Yang, J.; Jakob, G.; Mokrousov, Y.; Kläui, M. Harnessing Orbital-to-Spin Conversion of Interfacial Orbital Currents for Efficient Spin-Orbit Torques. *Phys. Rev. Lett.* **2020**, *125* (17), 177201.

(48) Ferreira, A.; Rappoport, T. G.; Cazalilla, M. A.; Castro Neto, A. H. Extrinsic Spin Hall Effect Induced by Resonant Skew Scattering in Graphene. *Phys. Rev. Lett.* **2014**, *112* (6), 066601.

(49) Van Tuan, D.; Marmolejo-Tejada, J. M.; Waintal, X.; Nikolić, B. K.; Valenzuela, S. O.; Roche, S. Spin Hall Effect and Origins of Nonlocal Resistance in Adatom-Decorated Graphene. *Phys. Rev. Lett.* **2016**, *117* (17), 176602.

(50) Balakrishnan, J.; Koon, G. K. W.; Avsar, A.; Ho, Y.; Lee, J. H.; Jaiswal, M.; Baeck, S.-J.; Ahn, J.-H.; Ferreira, A.; Cazalilla, M. A.; Castro Neto, A. H.; Özyilmaz, B. Giant Spin Hall Effect in Graphene Grown by Chemical Vapour Deposition. *Nat. Commun.* **2014**, *5* (1), 4748.

(51) Ribeiro, M.; Power, S. R.; Roche, S.; Hueso, L. E.; Casanova, F. Scale-Invariant Large Nonlocality in Polycrystalline Graphene. *Nat. Commun.* **2017**, *8* (1), 2198.

(52) Cresti, A.; Nikolić, B. K.; Garcia, J. H.; Roche, S. Charge, Spin and Valley Hall Effects in Disordered Grapheme. *Riv. del Nuovo Cim.* **2016**, *39* (12), 587–667.

(53) Kaverzin, A. A.; van Wees, B. J. Electron Transport Nonlocality in Monolayer Graphene Modified with Hydrogen Silsesquioxane Polymerization. *Phys. Rev. B* **2015**, *91* (16), 165412.

(54) Wang, Y.; Cai, X.; Reutt-Robey, J.; Fuhrer, M. S. Neutral-Current Hall Effects in Disordered Graphene. *Phys. Rev. B* **2015**, *92* (16), 161411.

(55) Rex B. McLellan. The Solubility of Carbon in Solid Gold, Copper, and Silver. *Scr. Metall.* **1969**, *3*, 389–392.

(56) López, G. A.; Mittemeijer, E. J. The Solubility of C in Solid Cu. *Scr. Mater.* **2004**, *51* (1), 1–5.

(57) Lan, Y.; Zondode, M.; Deng, H.; Yan, J.-A.; Ndaw, M.; Lisfi, A.; Wang, C.; Pan, Y.-L. Basic Concepts and Recent Advances of Crystallographic Orientation Determination of Graphene by Raman Spectroscopy. *Crystals* **2018**, *8* (10), 375.

(58) Biesinger, M. C. Advanced Analysis of Copper X-Ray Photoelectron Spectra. *Surf. Interface Anal.* **2017**, *49* (13), 1325–1334.

(59) Safeer, C. K.; Herling, F.; Choi, W. Y.; Ontoso, N.; Inglá-Aynés, J.; Hueso, L. E.; Casanova, F. Reliability of Spin-to-Charge Conversion Measurements in Graphene-Based Lateral Spin Valves. *2D Mater.* **2022**, *9* (1), 015024.

(60) Inglá-Aynés, J.; Groen, I.; Herling, F.; Ontoso, N.; Safeer, C. K.; De Juan, F.; Hueso, L. E.; Gobbi, M.; Casanova, F. Omnidirectional Spin-to-Charge Conversion in Graphene/NbSe₂ van der Waals Heterostructures. *2D Mater.* **2022**, *9* (4), 045001.

(61) Safeer, C. K.; Ontoso, N.; Inglá-Aynés, J.; Herling, F.; Pham, V. T.; Kurzmann, A.; Ensslin, K.; Chuvalin, A.; Robredo, I.; Vergniory, M. G.; De Juan, F.; Hueso, L. E.; Calvo, M. R.; Casanova, F. Large Multidirectional Spin-to-Charge Conversion in Low-Symmetry Semimetal MoTe₂ at Room Temperature. *Nano Lett.* **2019**, *19* (12), 8758–8766.

(62) Ontoso, N.; Safeer, C. K.; Herling, F.; Inglá-Aynés, J.; Yang, H.; Chi, Z.; Martin-Garcia, B.; Robredo, I.; Vergniory, M. G.; de Juan, F.; Reyes Calvo, M.; Hueso, L. E.; Casanova, F. Unconventional Charge-to-Spin Conversion in Graphene/MoTe₂ van der Waals Heterostructures. *Phys. Rev. Appl.* **2023**, *19* (1), 014053.

(63) Camosi, L.; Světlík, J.; Costache, M. V.; Sávero Torres, W.; Fernández Aguirre, I.; Marinova, V.; Dimitrov, D.; Gospodinov, M.; Sierra, J. F.; Valenzuela, S. O. Resolving Spin Currents and Spin Densities Generated by Charge-Spin Interconversion in Systems with Reduced Crystal Symmetry. *2D Mater.* **2022**, *9* (3), 035014.

(64) Gottardi, S.; Müller, K.; Bignardi, L.; Moreno-López, J. C.; Pham, T. A.; Ivashenko, O.; Yablonskikh, M.; Barinov, A.; Björk, J.; Rudolf, P.; Stöhr, M. Comparing Graphene Growth on Cu(111) versus Oxidized Cu(111). *Nano Lett.* **2015**, *15* (2), 917–922.

(65) Han, W.; McCreary, K. M.; Pi, K.; Wang, W. H.; Li, Y.; Wen, H.; Chen, J. R.; Kawakami, R. K. Spin Transport and Relaxation in Graphene. *J. Magn. Magn. Mater.* **2012**, *324* (4), 369–381.

(66) Ingla-Aynés, J.; Guimarães, M. H. D.; Meijerink, R. J.; Zomer, P. J.; van Wees, B. J. 24- μ m Spin Relaxation Length in Boron Nitride Encapsulated Bilayer Graphene. *Phys. Rev. B* **2015**, *92* (20), 201410.

(67) Rojas-Sánchez, J.-C.; Reyren, N.; Laczkowski, P.; Savero, W.; Attané, J.-P.; Deranlot, C.; Jamet, M.; George, J.-M.; Vila, L.; Jaffrès, H. Spin Pumping and Inverse Spin Hall Effect in Platinum: The Essential Role of Spin-Memory Loss at Metallic Interfaces. *Phys. Rev. Lett.* **2014**, *112* (10), 106602.

(68) Kim, J.; Sheng, P.; Takahashi, S.; Mitani, S.; Hayashi, M. Spin Hall Magnetoresistance in Metallic Bilayers. *Phys. Rev. Lett.* **2016**, *116* (9), 097201.

(69) Rojas Sánchez, J. C.; Vila, L.; Desfonds, G.; Gambarelli, S.; Attané, J. P.; De Teresa, J. M.; Magén, C.; Fert, A. Spin-to-Charge Conversion Using Rashba Coupling at the Interface between Non-Magnetic Materials. *Nat. Commun.* **2013**, *4* (1), 2944.

(70) Pham, V. T.; Yang, H.; Choi, W. Y.; Marty, A.; Groen, I.; Chuvalin, A.; Bergeret, F. S.; Hueso, L. E.; Tokatly, I. V.; Casanova, F. Large Spin-Charge Interconversion Induced by Interfacial Spin-Orbit Coupling in a Highly Conducting All-Metallic System. *Phys. Rev. B* **2021**, *104* (18), 184410.

(71) Rojas-Sánchez, J.-C.; Oyarzún, S.; Fu, Y.; Marty, A.; Vergnaud, C.; Gambarelli, S.; Vila, L.; Jamet, M.; Ohtsubo, Y.; Taleb-Ibrahimi, A.; Le Fèvre, P.; Bertran, F.; Reyren, N.; George, J.-M.; Fert, A. Spin to Charge Conversion at Room Temperature by Spin Pumping into a New Type of Topological Insulator: α -Sn Films. *Phys. Rev. Lett.* **2016**, *116* (9), 096602.

Supporting Information

Note 1 Methods.

Sample fabrication. Single layer graphene was exfoliated from bulk graphite crystals (supplied by NGS Naturgraphit GmbH) on Si substrates with 300 nm SiO₂. Calibrated optical microscopy was used to identify the number of layers. The device was then fabricated with 4 e-beam lithography steps. First, the graphene was patterned into several Hall bars with a width of 500 nm using e-beam lithography. 20-nm-thick Al deposited by high-vacuum thermal evaporation (base pressure $\sim 7 \times 10^{-7}$ torr) was used as a hard mask, then the graphene was reactive-ion etched using an Ar/O₂ plasma. The Al hard mask was removed with a base developer solution with tetra-methyl ammonium hydroxide, followed by annealing of the device at 400°C for 1 hour in ultra-high vacuum ($\sim 2 \times 10^{-8}$ torr) to remove residues from the graphene. Second, a 5-nm-thick Cu layer was deposited in the cross-junction of the graphene Hall bar using e-beam lithography, ultra-high vacuum thermal evaporation (base pressure $< 1.2 \times 10^{-9}$ torr), and lift-off process. The device was left in atmosphere for 72 hours for oxidization. Third, graphene was contacted with non-magnetic Pd(5 nm)/Au(45 nm) contacts fabricated using e-beam lithography followed by e-beam evaporation and lift-off. Finally, the magnetic TiO_x/Co electrodes were fabricated by e-beam lithography, deposition of 2.6 Å of Ti (followed by oxidation in air for 10 minutes), 35 nm of Co, and 10 nm of Au as capping layer by e-beam evaporation, and lift-off. The width of the magnetic electrodes are 150 nm or 300 nm in order to have different coercivity. The optical images of the devices during each fabrication step are shown in Fig. S8.

Optical measurements. Raman spectroscopy characterization was carried out in an Alpha 300R Confocal Raman WITec microscope using a 532 nm laser (incident power < 1 mW to avoid damage to the samples during the Raman spectra acquisition), a diffraction grating of 600 l/mm and 100 \times objective (N.A. 0.90).

Electrical measurements. The transport measurements are performed in a physical property measurement system (PPMS) by Quantum Design using a DC reversal technique with a Keithley 2182 nanovoltmeter and a 6221 current source. The n-doped Si substrate acts as a back-gate electrode to which we apply the gate voltage across 300 nm of SiO₂ with a Keithley 2636A.

Note 2 Spin precession fitting process.

1. Symmetric Hanle fitting by considering the low contact resistance of the TiO_x/Co contact.

To analyze the symmetric Hanle precession experiments obtained while having a parallel and or antiparallel orientation of the Co magnetization, we model the spin propagation in our devices using the Bloch equations:

$$D_s \nabla^2 \vec{\mu} - \frac{\vec{\mu}}{\tau_s} + \vec{\omega} \times \vec{\mu} = 0 \quad (1)$$

where $\vec{\mu}$ is the spin accumulation, D_s the spin diffusion constant, and τ_s the spin lifetime. $\vec{\omega} = g\mu_B \vec{B}$ is the Larmor frequency, $g=2$ is the Landé factor, μ_B is the Bohr magneton, and \vec{B} is the applied magnetic field.

The spin precession is induced in the $y - z$ plane when applying a magnetic field along x direction. In this case, Eq. (1) turns into

$$D_s \frac{d^2}{dx^2} \begin{pmatrix} \mu_x \\ \mu_y \\ \mu_z \end{pmatrix} - \begin{pmatrix} \tau_x^{-1} \\ \tau_y^{-1} \\ \tau_z^{-1} \end{pmatrix} \begin{pmatrix} \mu_x \\ \mu_y \\ \mu_z \end{pmatrix} + \vec{\omega} \begin{pmatrix} 0 \\ \mu_y \\ -\mu_z \end{pmatrix} = 0 \quad (2)$$

The solution of μ_y and μ_z in Eq. (2) is

$$\mu_y = A e^{\frac{x}{\lambda_s} \sqrt{1+i\omega\tau_s}} + B e^{\frac{x}{\lambda_s} \sqrt{1-i\omega\tau_s}} + C e^{-\frac{x}{\lambda_s} \sqrt{1+i\omega\tau_s}} + D e^{-\frac{x}{\lambda_s} \sqrt{1-i\omega\tau_s}} \quad (3)$$

$$\mu_z = -iA e^{\frac{x}{\lambda_s} \sqrt{1+i\omega\tau_s}} + iB e^{\frac{x}{\lambda_s} \sqrt{1-i\omega\tau_s}} - iC e^{-\frac{x}{\lambda_s} \sqrt{1+i\omega\tau_s}} + iD e^{-\frac{x}{\lambda_s} \sqrt{1-i\omega\tau_s}} \quad (4)$$

where $\lambda_s = \sqrt{\tau_s D_s}$ is the spin diffusion length. A, B, C and D are the coefficients determined by the boundary conditions. The spin current is defined as:

$$I_{Sy(z)} = -\frac{W_{gr}}{eR_{\square}} \frac{d\mu_y(z)}{dx}, \quad (5)$$

where W_{gr} is the width of the graphene channel and R_{\square} is the square resistance of graphene. The spin accumulation at the detection position $x = x_{det}$ is then converted into a voltage with

$$V_{det}^s = P \frac{\mu_y(x_{det})}{e}, \quad (6)$$

where P is the spin polarization of the Co detector. We consider that the Co injector has the same spin polarization. V_{det}^s is usually normalized by the charge current I_c , giving the non-local resistance

$$R_{NL} = \frac{V_{det}^s}{I_c}. \quad (7)$$

The non-local resistance is also affected by the contact pulling effect¹. Because of the finite/small in-plane shape anisotropy of the ferromagnetic electrodes, the magnetization is then pulled by an angle β from their easy axis towards the field direction, injecting spins along x and resulting in an additional term to the non-local resistance. The R_{NL} obtained in this case is

$$R_{NL} = \pm R^s \cos(\beta_1) \cos(\beta_2) + R^{s0} \sin(\beta_1) \sin(\beta_2). \quad (8)$$

Here \pm represents the non-local signal with parallel (P) and antiparallel (AP) configuration of the Co electrode magnetizations. β_1 and β_2 correspond to the angle β of the two magnetic electrodes used as injector and detector. For simplicity, we consider that the two Co electrodes have the same pulling effect with the angle, $\beta = \beta_1 = \beta_2$. R^{s0} is a constant that corresponds to the spin signal at zero magnetic field. The net spin signal ΔR_{NL} is then expressed as:

$$\Delta R_{NL} = \frac{R_{NL}^P - R_{NL}^{AP}}{2} = R^s \cos^2(\beta). \quad (9)$$

Because of the opposite spin precession sign of R_{NL}^P and R_{NL}^{AP} , the sum $R_{sum} = R_{NL}^P + R_{NL}^{AP}$ is then proportional to $\sin^2(\beta)$. For our analysis, we used the contact pulling from the measurement points on the curve of R_{sum} vs. B .

We thus determine the spin signal using the following boundary conditions:

1. Spin accumulation μ is continuous.
2. Spin current is continuous except:
 - a. At F1 with spin injection by the charge current, by $\Delta I_s = I_c \cdot P/2$;
 - b. At F1 and F2 due to the spin backflow effect because of the low contact resistance, by $\Delta I_s = -\mu_s/(2eR_c)$, where R_c is the contact resistance.
3. Spin current is zero at the sample ends.

We write these boundary conditions in a matrix X which fulfills: $MX = Y$, where M contains the coefficients $M = A, B, C \dots$ and $Y = (0, \dots, \frac{I_c P}{2}, 0, \dots)$ and use the Moore-Penrose inverse to invert X^{-1} and obtain $M = YX^{-1}$. Using the numeric solution described above, we input the measured net spin signal ΔR_{NL} , square resistance R_{\square} , pulling factor $\cos^2(\beta)$, channel size W_{gr} determined by SEM, and the contact resistance R_c .

As our graphene is directly on SiO_2 , the small free mean path enables us to neglect the spin diffusivity decrease sourcing from the electron-electron scattering and assume that the spin and charge diffusion coefficients are equal²⁻⁴. To decrease the number of fitting parameters, therefore, we fix the charge diffusion coefficient (D_c), extracted with

$$D_c = \frac{\hbar v_{F0}}{2e^2 R_{\square}} \sqrt{\frac{\pi}{|n|}}. \quad (10)$$

Here, $v_{F0}=10^6$ m/s is the Fermi velocity, \hbar is the reduced Planck constant, n is the carrier density determined with

$$n = \epsilon_0 \epsilon_{SiO2} (V_g - V_{CNP}) / e \cdot d_{SiO2} \quad (11)$$

with ϵ_0 being the vacuum permittivity, $\epsilon_{SiO_2} = 3.9$ for SiO_2 relative dielectric permittivity, d_{SiO_2} is the thickness of SiO_2 of 300 nm. We then fit the polarization P and the spin lifetime τ_s^{Gr} of pristine graphene.

2. Antisymmetric spin precession fitting for SHE and ISHE signals.

We determine the spin Hall angle θ_{SH} and the spin lifetime $\tau_s^{CuOx/gr}$ of the graphene in the heterostructure with the antisymmetric spin precession signal ΔR_{ISHE} originated from the (inverse) spin Hall effect of functionalized graphene. Here, we derive the ISHE but, due to reciprocity, the obtained equation is valid for both configurations. The non-local resistance ΔR_{ISHE} is given by

$$\Delta R_{ISHE} = \frac{\theta_{SH} R_{\square} \overline{I_{Sz}}}{I_c} \cdot \cos(\beta) \quad (12)$$

where $\overline{I_{Sz}}$ is the average spin current in the cross-junction area of the Hall bar, which is defined as $\overline{I_{Sz}} = \frac{1}{W_{cr}} \int_L^{L+W_{cr}} I_{Sz}(x) dx$, where L is the distance from F1 electrode to the edge of the Hall cross and W_{cr} is the width of the cross. $\cos(\beta)$ is the term indicating the contact pulling of the ferromagnetic electrode. Note that, since there is only one magnetic electrode, this term is not squared as in Eq. (9). To determine $I_{Sz}(x)$, we use the equations and boundary conditions described in Section 7.1. Finally, since the CNP is the same for the pristine and CuO_x -covered regions (see Fig. S12), we assume the charge diffusion coefficients for the CuO_x -covered region and the pristine region to be equal.

Note 3: XPS analysis.

X-ray photoemission spectroscopy (XPS) was employed to investigate the oxidation of the 5-nm-thick Cu film used in the device fabrication. In order to judge the behavior observed in the devices, two additional samples were initially prepared under ultra-high vacuum (UHV) conditions, one with a low coverage of 0.8 nm and a second one with a higher coverage of 3 nm of Cu. The XPS of these two samples, which were successively exposed to air, were then compared to the 5-nm-thick Cu film (equivalent to the conditions of the device). The substrate material for Cu deposition was graphite (HOPG), which was exfoliated in the fast-entry chamber ($p = 1 \times 10^{-8}$ mbar) and additionally heated to 400 °C. The low energy electron diffraction (LEED) pattern of the graphite was a circle indicating the existence of multiple graphite domains within the LEED spot area. The XPS reference spectrum showed no trace of oxygen or other impurities (Fig. S2, top panels).

In the next step, pure Cu (99.999% purity) was evaporated at a rate of approximately 0.1 nm per minute. The pressure during evaporation was always kept below $p = 5 \times 10^{-9}$ mbar. After Cu deposition, the samples were transferred without leaving the UHV environment to the XPS chamber.

The evolution of the oxidation of the low coverage sample was investigated by measuring the XPS spectra prior and after different air exposure times: 1 h, 24 h and 72 h. Air exposure means here that the sample was kept in the laboratory at room temperature and at ambient relative humidity of approx. 60%. The high coverage sample was measured before and after 72 h air exposure to directly compare with the 5-nm-thick Cu film prepared at the same conditions as the Cu film employed for device fabrication.

X-ray photoelectron spectroscopy was carried out holding the sample at room temperature and illuminating it with monochromatized Al K α light ($h\nu = 1486.6$ eV) from a microfocus setup (SPECS Focus 600). The excited photoelectrons were collected by a SPECS 150 hemispherical analyzer at emission and incidence angles of 40° and 60°, respectively. The overall experimental resolution was extracted from Fermi edge analysis of a reference gold sample and resulted in 0.4 eV. The Fermi level position of the reference sample was subtracted to get core level emission in binding energy.

Survey. The survey XPS spectrum of the 5-nm-thick Cu on top of graphite after an air exposure of 72 h is shown in Fig. S1. The different peaks are identified and compared to a reference Cu₂O spectrum⁵. The survey reveals that there are no other atomic species apart from the expected Cu, O and C.

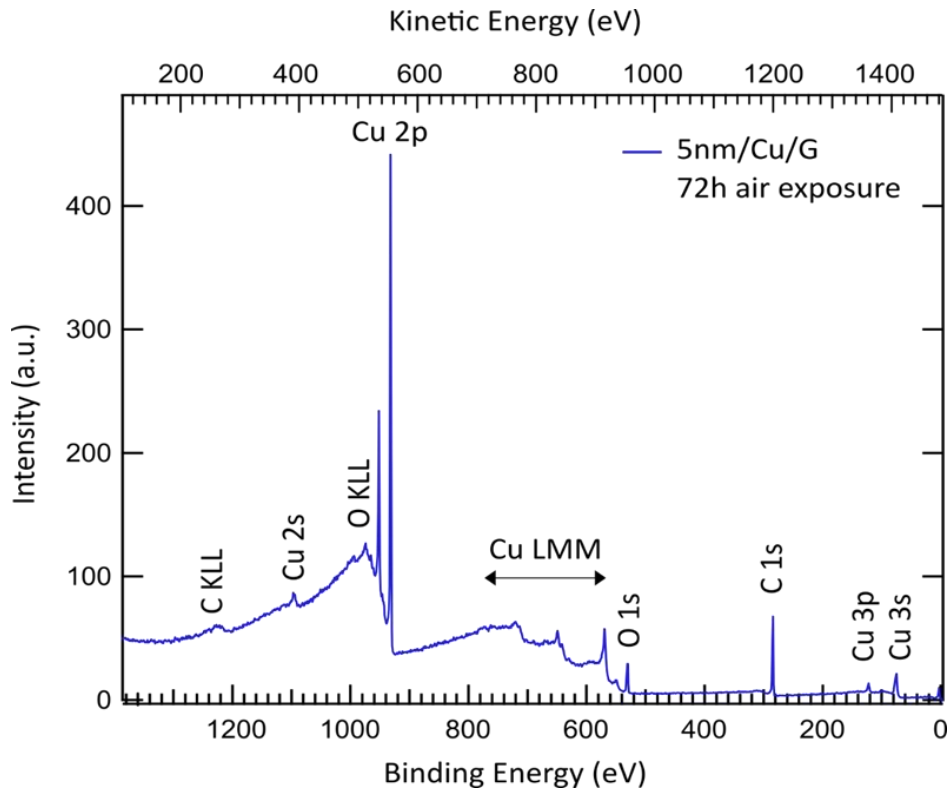


Fig. S1. Survey. XPS survey spectrum of a 5-nm-thick Cu film grown on top of graphite and left in air 72 h prior to the measurement. This film was grown exactly under the same experimental conditions as the samples employed to fabricate the devices.

The devices were fabricated using the same Cu coverage and air exposure conditions. For reference, XPS analysis has been performed for Cu deposited on top of exfoliated graphite, while the Cu in the devices was grown on top of exfoliated graphene. According to XPS results, the reference sample of Cu on top of HOPG does not grow as a continuous homogeneous film but follows the inhomogeneities of the HOPG substrate. This leads to the fact that after deposition of a 5-nm-thick Cu, we are still able to detect the C 1s signal of the HOPG substrate. If a 5-nm-thick Cu film would have homogeneously and fully covered the sample, only a very small C signal would have been observed due to the reduced mean free path of the photoelectrons at the approx. 1200 eV kinetic energy. Additionally, the different Cu quantity measured for different sample positions points out that the Cu growth on exfoliated graphite is not homogeneous. For the flatter graphene substrate, however, the Cu growth was more homogenous, as reflected by the experimental AFM measurements (see Fig. 1c of the main text).

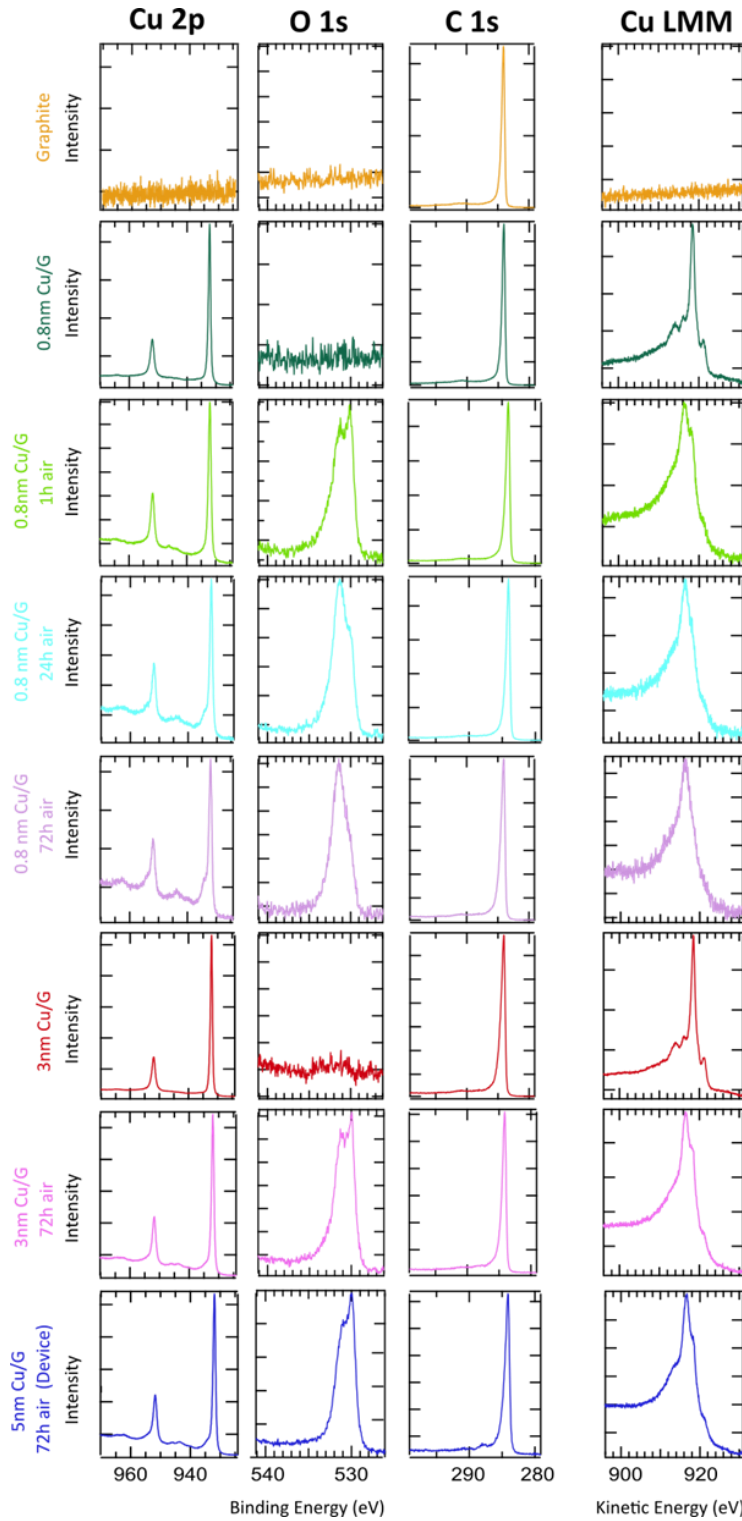


Fig. S2. XPS summary. XPS spectra of Cu 2p, Cu LMM, O 1s and C 1s measured for graphite (reference), for a 0.8-nm-thick Cu in UHV, after 1 h, 24 h and 72 h air exposure; for a 3-nm-thick Cu in UHV and after 72 h in air; and for a 5-nm-thick film prepared in the same way as the device after 72 h air exposure.

Cu 2p levels. The graphs of Fig. S3 show the Cu 2p core level split into the $2p_{1/2}$ and $2p_{3/2}$ sub-levels due to the spin-orbit interaction. In Fig. S3(a), the evolution of the 0.8-nm-thick Cu sample

prior and after air exposure is observed. After 1 h air exposure, the film signal decreases significantly due to the presence of air contamination on the surface. The signal continues decreasing with increasing the air exposure time. The binding energies of the Cu 2p_{1/2} and 2p_{3/2} levels for the 0.8-nm-thick Cu in UHV are 952.0 eV and 932.1 eV, respectively, in agreement with the reported values for metallic Cu(0)⁶. After 1 h air exposure, the 2p levels move slightly to lower binding energies, 951.9 eV and 932.0 eV. There is no further shifts after 24 h and 72 h air exposure times. Although the observed shift to lower binding energies is very small, 0.1-0.2 eV, it reflects the oxidation of the Cu, resulting in Cu₂O (Cu(I) species). For the 0.8-nm-thick sample after 24 h/72 h air exposure, there is a broad peak that emerges around 954.2 eV and 934.3 eV. This emission is related to the appearance of Cu(OH)₂. In Fig. S3(b), the sample of 3-nm-thick Cu film grown in UHV and after 72 h air exposure is shown. Similar to the low coverage sample, there is a tiny shift to lower binding energies of the Cu 2p_{1/2} and 2p_{3/2} peaks after 72 h air exposure and the additional contribution of the Cu(OH)₂ is also present for the air exposed sample. Finally, in Fig. S3(c), we compare the spectra for all three samples of different Cu coverages after 72 h air exposure. The binding energies of the core levels are the same. Additionally, we observe that the amount of Cu measured for the 3-nm-thick and the 5-nm-thick is practically the same. This is related to fact that the escape depth of the photoelectrons is smaller than the film thickness and we are reaching the “saturation limit” of XPS.

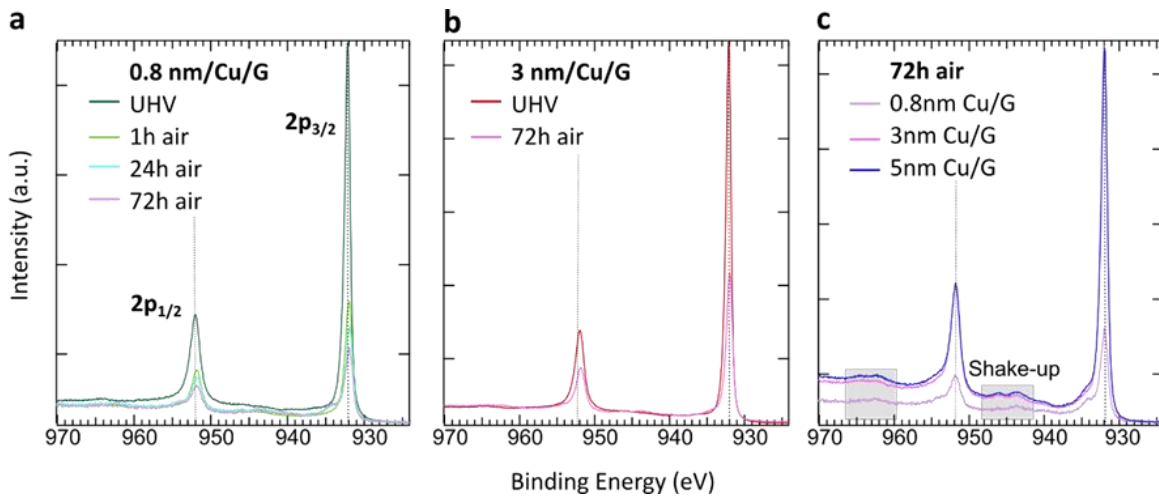


Fig. S3. Cu 2p. Cu 2p_{1/2} and 2p_{3/2} levels for: (a) the low coverage 0.8-nm-thick sample after different air exposure times; (b) the high coverage 3-nm-thick sample in UHV and after 72 h in air, (c) comparison between the different coverages (0.8 nm, 3 nm, and 5 nm of Cu) after 72 h in air.

The Cu quantity on the surface has been estimated as follows. The kinetic energy of the photoemitted electrons of the Cu 2p_{3/2} level is $E_{kin} = 553.95$ eV. Therefore, the mean free-path of these electrons⁷ is $\lambda = \frac{43}{E^2} + 0.054\sqrt{E} = 1.27$ nm. Comparing the integrals obtained by fitting the peaks with Lorentzian functions and considering that the intensity decreases exponentially as $I = I_0 e^{-\frac{z}{\lambda}}$, we obtained that there is a 2.2 nm difference between the low and high coverages UHV samples, which is in agreement with the QMB reading.

For the air-exposed samples, there are shake-up peaks around 962-964 eV and 944-946 eV, respectively (shadowed areas in Fig. S10(c)). These emissions are related to the d^9 configuration of the Cu(II) species, pointing out that there is a small quantity of Cu(II) on the surface. There is

no evidence of the presence of CuO in the sample, since 2p peaks related to this compound would be expected at binding energies 933.1 eV and 953 eV. Thus, we can conclude that the Cu(II) species comes from Cu(OH)₂. This conclusion is supported by the analysis of the Auger Cu LMM lines and the O 1s spectra.

Cu LMM. Figure S4(a) shows the evolution of the Cu L₃M_{4,5}M_{4,5} spectra for the 0.8-nm-thick Cu sample with different air exposure times. For the UHV sample, 6 different peaks can be identified at different kinetic energies, each one with a different intensity, and in complete agreement with the Auger reference spectrum for metallic Cu(0)⁸.

UHV 0.8nm sample	P1	P2	P3	P4	P5	P6
E_{Kin} (eV)	921.2	919.6	918.5	918.0	916.1	914.1

After air exposure, the Auger spectra changes completely. The peaks related to Cu(0) disappear and, in the oxidized spectra, the following new lines appear:

Air exposed 0.8nm sample	P'1	P'2	P'3
E_{Kin} (eV)	921.5	918.1	916.4

There is not a big difference between the spectra after 1 h, 24 h and 72 h of air exposure, suggesting that the main surface oxidation occurs within the first hour. Additionally, the peaks of the air-exposed sample spectra are quite broad, indicating that there are contributions from Cu(I) and Cu(II) species. Again, a comparison with the Auger lines reported for Cu₂O, CuO and Cu(OH)₂, indicates the presence of Cu₂O and Cu(OH)₂ on the surface.

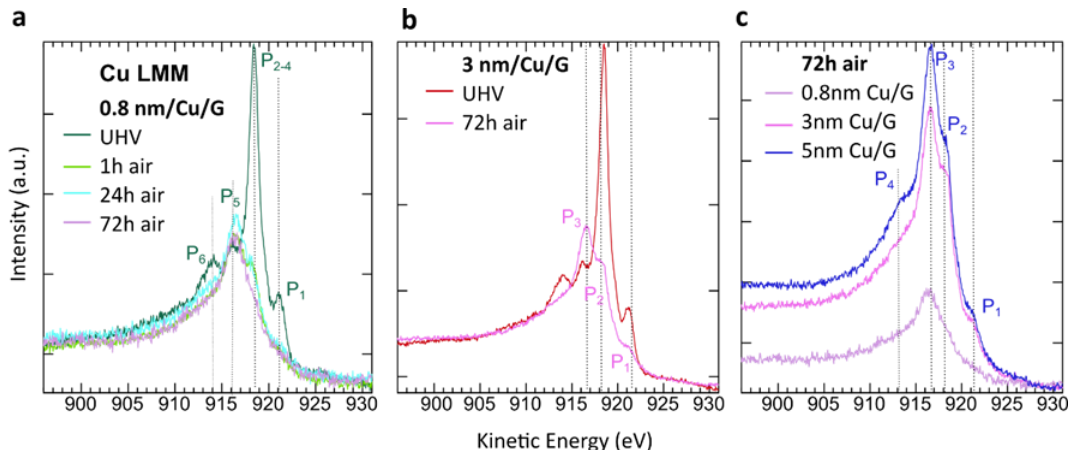


Fig. S4. Auger Cu LMM. Cu L₃M_{4,5}M_{4,5} spectra for: (a) the low coverage 0.8-nm-thick sample after different air exposure times; (b) the high coverage 3-nm-thick sample in UHV and after 72 h in air, (c) a comparison between the different coverages (0.8 nm, 3 nm, and 5 nm of Cu) after 72 h in air.

In Fig. S4(b), it is clear that the peaks related to the metallic Cu(0) in the UHV 3-nm-thick Cu sample are completely replaced by at least 3 peaks for the sample left in air for 72 h. A complete oxidation of the Cu species happened. Lastly, a comparison between the three samples with different Cu coverages after 72 h of air exposure is shown in Fig. S4(c). In this case, a fourth peak

is more visible for the 5-nm-thick sample with a kinetic energy of 913.5 eV, characteristic of the Cu_2O .

O 1s level. Figure S5 shows the XPS spectra of the O 1s levels for the different samples. In Fig. S5(a) we observe that there is no O in the exfoliated graphite and in the Cu film grown in UHV conditions. After 1 h of air exposure, two main peaks appear in the spectrum, one at a binding energy of 530.0 eV, which is associated to the Cu_2O , and a second one at 531.4 eV, which is related to $\text{Cu}(\text{OH})_2$. The hydroxide-related peak is much broader, suggesting that it probably includes other contributions apart from the $\text{Cu}(\text{OH})_2$. After 24 h and 72 h of air exposure, the intensity of both peaks increases, becoming the hydroxide peak the most intense one. Table S1 summarizes the employed fit parameters.

Figure S5(e) compares the O 1s spectra of the 0.8-nm-, 3-nm-, and 5-nm-thick Cu samples after 72 h oxidations. For the higher coverages, the most intense contribution arises from Cu_2O .

C 1s level. Figure S6 shows the evolution of the C 1s peak for the different investigated samples. In Fig. S6(a), we observe how the signal of the C decreases after Cu deposition and, in Fig. S6(b), we see how the signal further decreases with air exposure times. There is no evidence of C oxidation in these spectra. In Fig. S6(c), a comparison between the spectra of the 0.8-nm-, 3-nm-, and 5 nm-thick Cu samples after 72 h of oxidation is shown.

To summarize, from the XPS analysis we observe a complete oxidation of the metallic $\text{Cu}(0)$ into $\text{Cu}(\text{I})$ and $\text{Cu}(\text{II})$ species, arising from Cu_2O and $\text{Cu}(\text{OH})_2$.

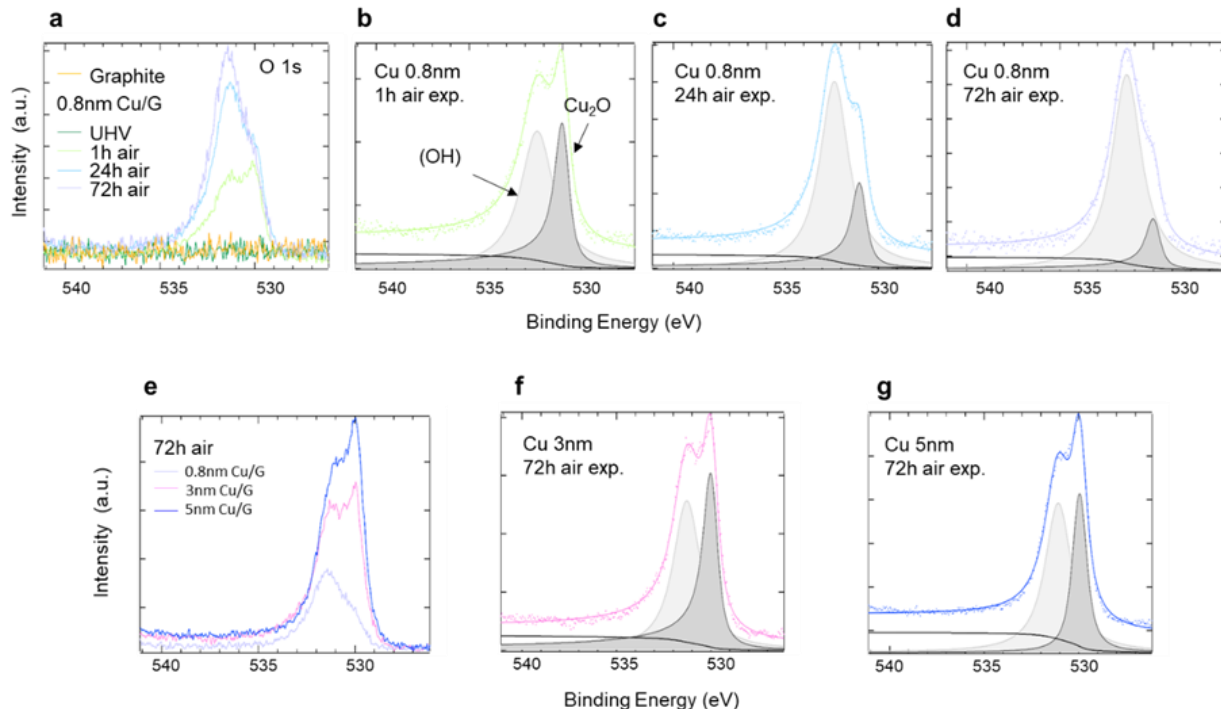


Fig. S5. O 1s spectra for: (a) pristine graphite and 0.8-nm-thick Cu in UHV and after different air exposure times; Fits of the O 1s levels for the 0.8-nm-thick sample after (b) 1 h, (c) 24 h and (d) 72 h of air exposure; (e) comparison

between the different coverages after 72 h of air exposure. Fits of the O 1s levels for the (f) 3-nm-thick sample and (g) 5-nm-thick sample after 72 h of air exposure.

Coverage/Air exposure	Fit Parameters	P1 (Cu ₂ O)	P2 (Hydroxide)
1 nm after 1 h air exp.	E _{Bin} Position (eV)	530.0	531.4
	FWHM (eV)	0.29	1.04
	Integral	2.32	3.34
1 nm after 24 h air exp.	E _{Bin} Position (eV)	530.0	531.3
	FWHM (eV)	0.29	0.88
	Integral	2.27	6.71
1 nm after 72 h air exp.	E _{Bin} Position (eV)	530.0	531.4
	FWHM (eV)	0.29	0.90
	Integral	1.47	7.79
3 nm after 72 h air exp.	E _{Bin} Position (eV)	530.0	531.3
	FWHM (eV)	0.29	0.82
	Integral	12.04	12.88
5 nm after 72 h air exp.	E _{Bin} Position (eV)	530.0	531.1
	FWHM (eV)	0.34	0.78
	Integral	9.28	16.62

Table S1. Main fit parameters of the O1s level.

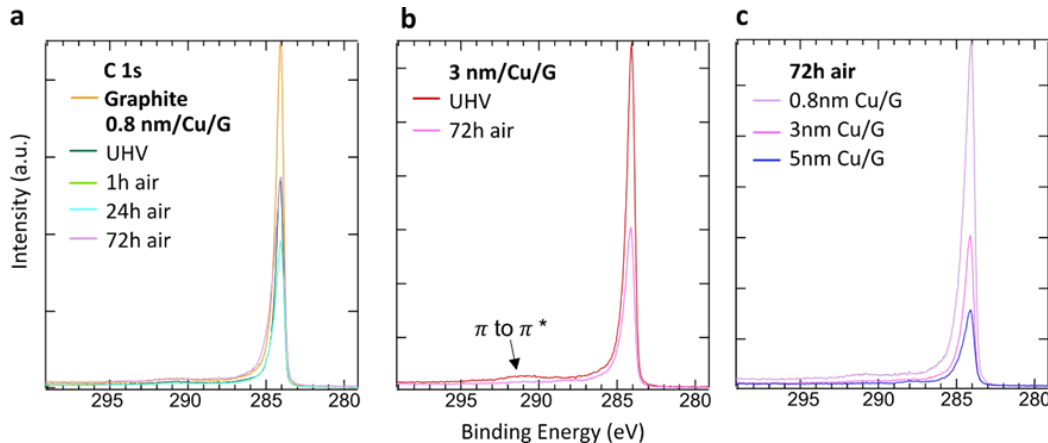


Fig. S6. C 1s spectra for: (a) pristine graphite and 0.8-nm-thick Cu in UHV and after different air exposure times; (b) 3-nm-thick Cu in UHV and after 72 h of air exposure; (c) comparison between the different coverages after 72 h of air exposure.

Supporting Figures.

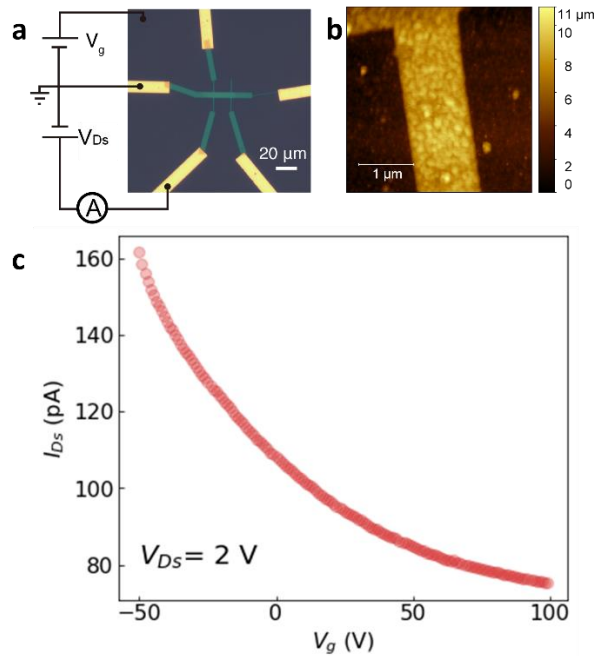


Fig. S7 Electrical characterization of oxidized copper. (a) Optical image of a 5-nm-thick Cu Hall bar device grown on a SiO_2 substrate, after ambient oxidation and contacted with Ti/Au electrodes. The transport measurement configuration is labeled. (b) AFM image of the oxidized Cu device shows a continuous morphology similar to that grown on graphene and shown in Fig. 1(c) of the main text. (c) Drain-source current (I_{DS}) as a function of the back gate voltage (V_g) measured at a drain-source voltage (V_{DS}) of 2 V and 300 K. One can observe that CuO_x exhibits an insulating behavior. The conductivity of CuO_x is at least seven orders of magnitude smaller than that of the graphene used in our experiment.

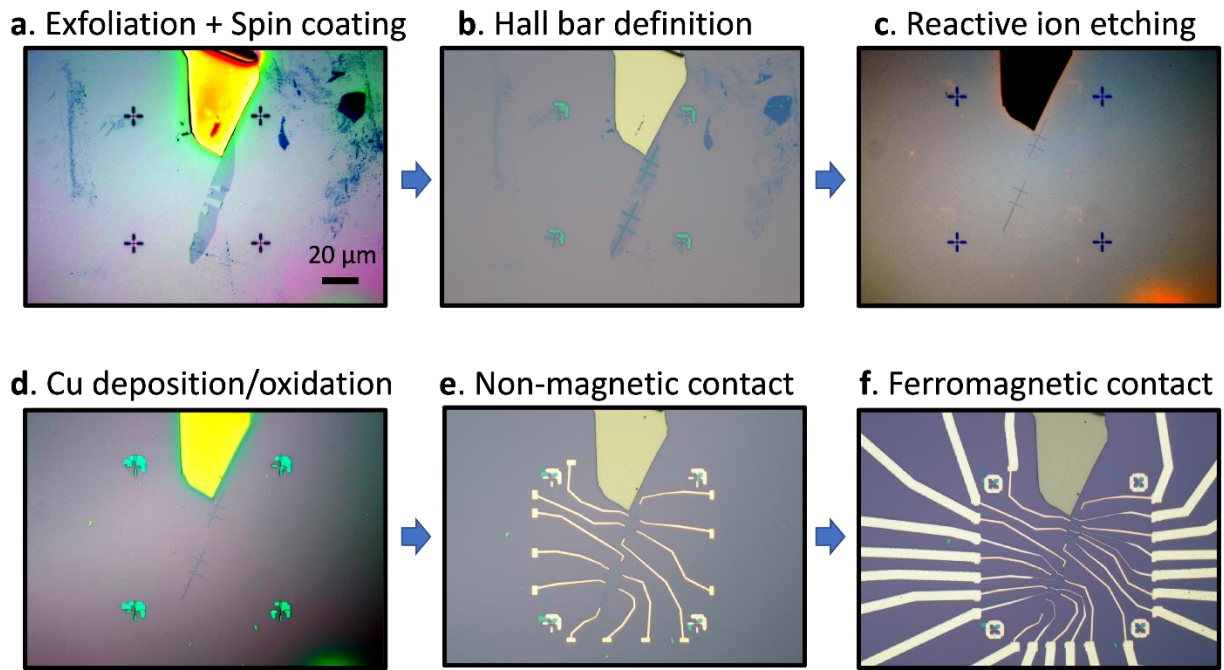


Fig. S8 Optical image of devices during the fabrication process. Optical image of Sample 1 and Sample 2 during the fabrication process. (a) Exfoliated single layer graphene on the substrate; (b) Hall bar definition with an Al hard mask; (c) graphene Hall bar after reactive ion etching; (d) Cu deposition on the cross-junction of the Hall bar, followed by ambient oxidation; (e) Non-magnetic Pd/Au contacts deposition; (f) Ferromagnetic TiO_x/Co contacts deposition.

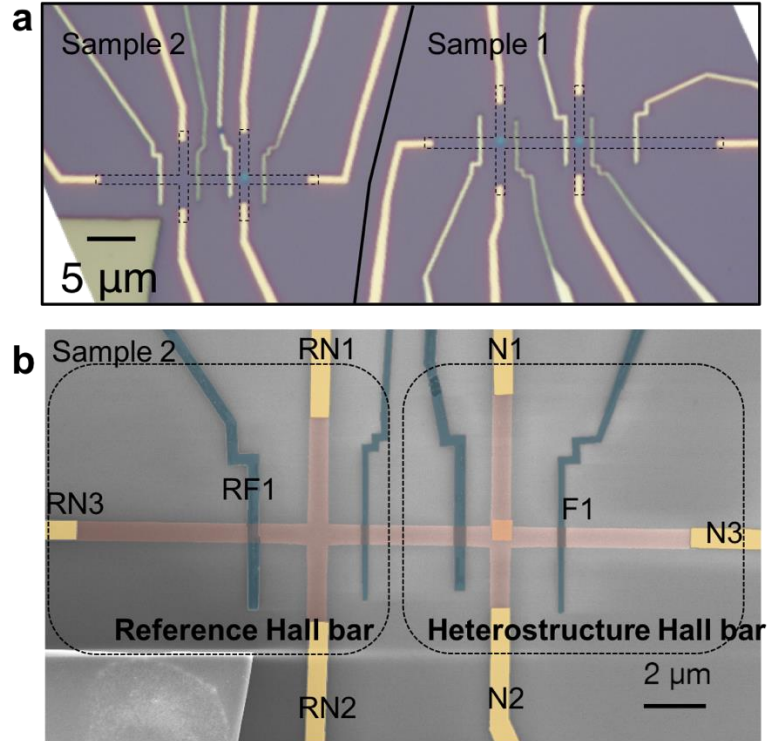


Fig. S9 Optical and SEM images of Sample 2. (a) Optical image of Sample 2. The optical image of Sample 1 is also included here, as the two samples are fabricated with the same single layer flake of graphene. The dashed lines indicate the edges of the graphene channel. (b) False-colored SEM image of Sample 2, which includes two non-local Hall bars named reference Hall bar and heterostructure Hall bar, respectively. The reference Hall bar does not have CuO_x covering the cross-junction area. The non-magnetic contact pads (N1 to N3 and RN1 to RN3) and magnetic electrodes (F1 and RF1) are indicated. The data shown in Fig. 4(a) of the main text is measured by applying current from F1 to N3 and detecting the non-local voltage between N1 and N2.

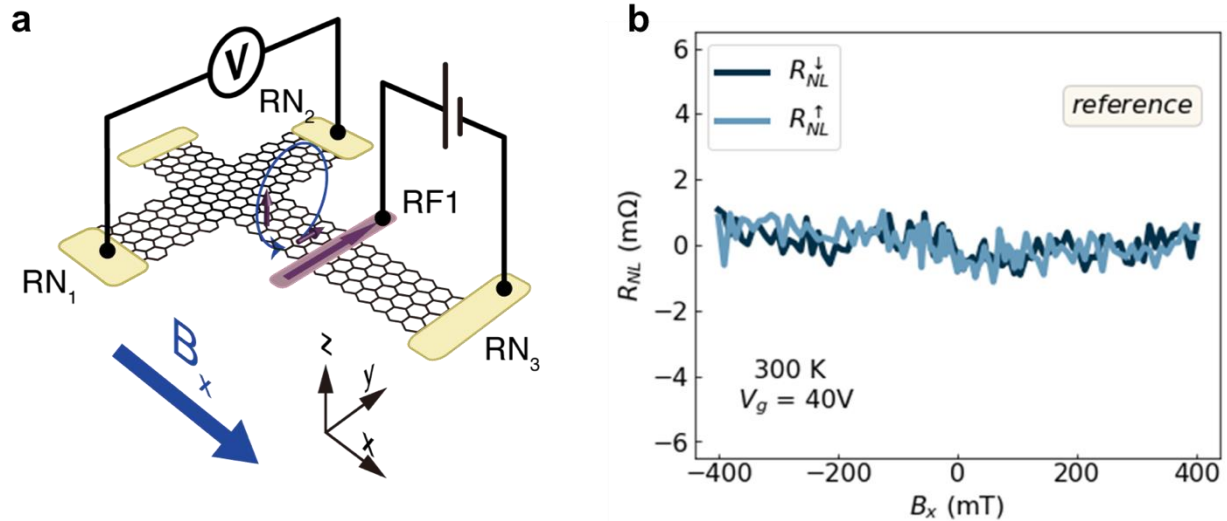


Fig. S10 Reference non-local Hall bar without CuO_x . (a) Measurement configuration for the reference non-local Hall bar in Sample 2, without CuO_x covering the cross-junction of the Hall bar. (b) Non-local resistance as a function of B_x using configuration in (a), with initial positive (R_{NL}^\uparrow , light-blue line) and negative (R_{NL}^\downarrow , dark-blue line) magnetization direction of RF1. Data is taken at 300 K and $V_g = 40$ V, the same condition as the data shown in Fig. 4(a) of the main text. The y -axis range is also set to be the same as in Fig. 4(a). We removed the baseline here for a better comparison. No evidence of spin-to-charge conversion is observed when there is no CuO_x on the cross-junction.

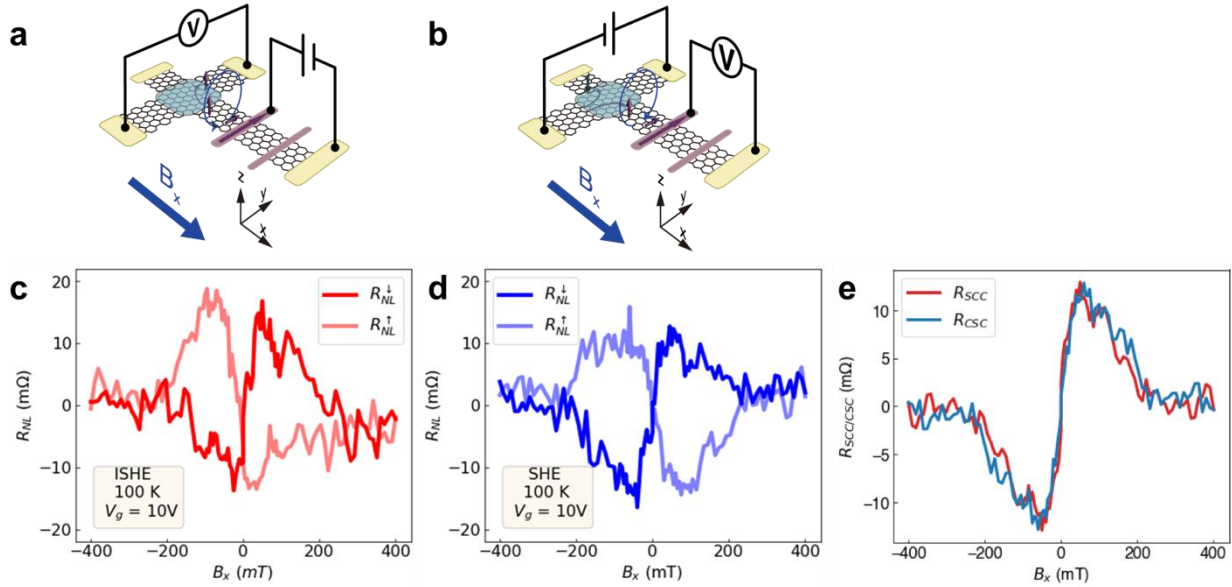


Fig. S11 Reciprocity between spin Hall effect and inverse spin Hall effect. Measurement configuration for antisymmetric Hanle precession with (a) spin-to-charge and (b) charge-to-spin conversion at the CuO_x-covered graphene and (a) spin injection and (b) detection using a FM electrode, with the results of Sample 1 measured at 100 K and $V_g = 10$ V shown in (c) and (d), respectively. The baseline is removed and the y -axis range is the same for comparison. (e) Net antisymmetric precession signal extracted from the data in (c) (red curve) and (d) (blue curve) by taking $R_{SCC/CSC} = (R_{NL}^\uparrow - R_{NL}^\downarrow)/2$ and antisymmetrizing it. The same amplitude and shape of the precession profile for the SHE and ISHE is obtained, in agreement with the Onsager reciprocity relations for the spin precession process, as has been discussed in the Supplementary Information S5 of Ref. ⁹.

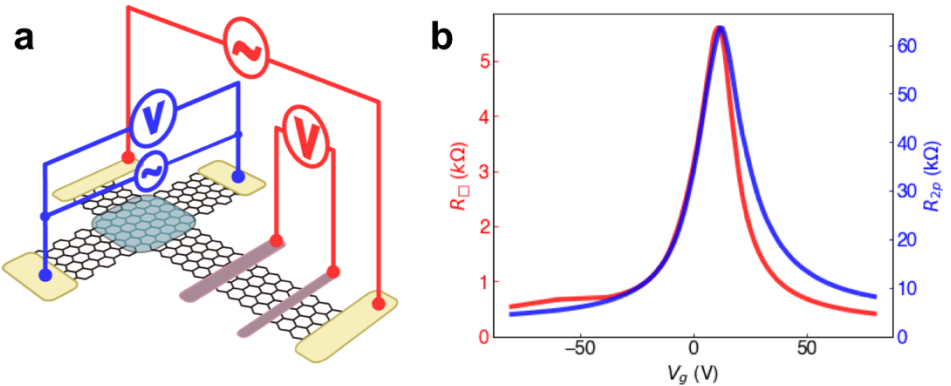


Fig. S12 Charge transport properties of the pristine graphene and the CuO_x-covered graphene. (a) Measurement configuration for the resistance of the pristine graphene (4-point resistance, in red) and the CuO_x-covered graphene at the cross-junction of the Hall bar (2-point resistance, in blue). (b) Square resistance of pristine graphene (red solid line) and 2-point resistance of the CuO_x-covered graphene at the cross-junction of the Hall bar (blue solid line) measured in Sample 1. The CNPs for both configurations are the same, indicating that both the CuO_x-covered graphene and the pristine graphene exhibit almost the same doping.

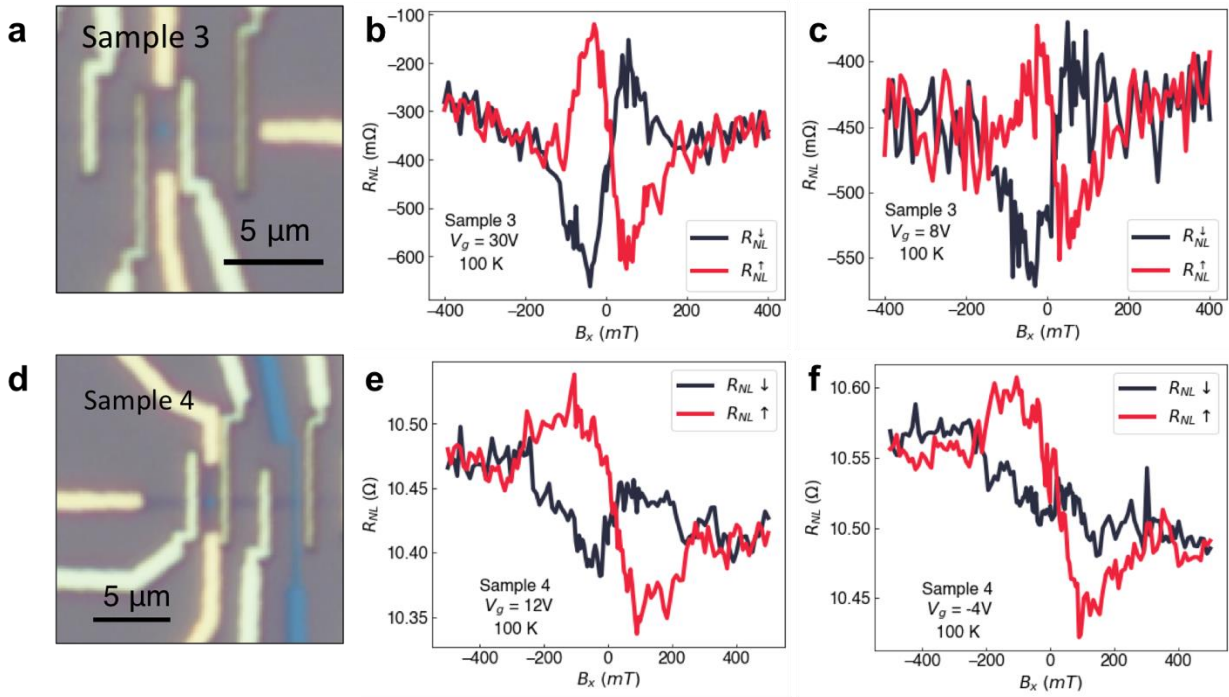


Fig. S13 Reproducibility. (a) Optical image of Sample 3. This sample is also fabricated with CuO_x on single layer graphene. (b),(c) Two representative charge-to-spin conversion curves measured at 100 K with $V_g = 30$ V and 8 V, respectively. The signal shows a clear antisymmetric component, indicating the detection of the SHE in the CuO_x /graphene heterostructure. (d) Optical image of Sample 4. The sample is fabricated with CuO_x on trilayer graphene. (e),(f) Two representative charge-to-spin conversion curves measured at 100 K with $V_g = 12$ V and -4 V, respectively.

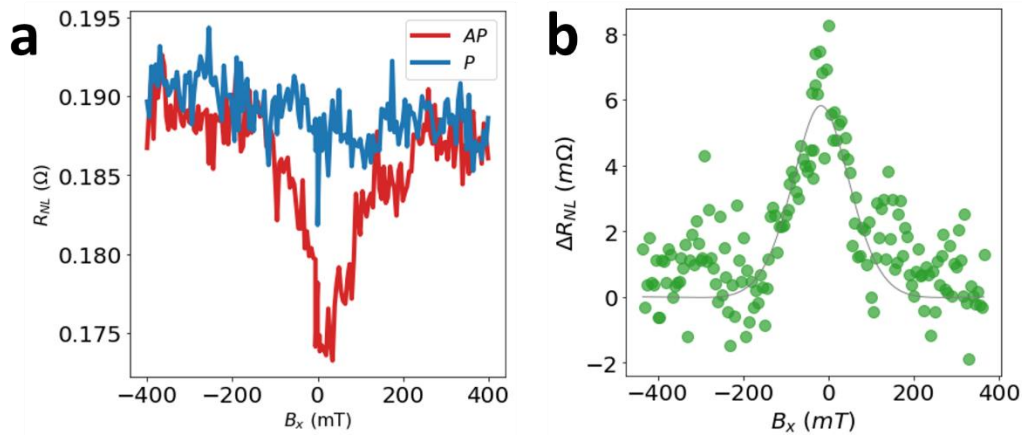


Fig. S14 Cross-section Hanle precession. (a) Non-local resistance across the $\text{CuO}_x/\text{graphene}$ region as a function of B_x measured at 300 K and $V_g = 0$ V, with the FM electrodes set in a parallel (R_{NL}^P , blue line) and antiparallel (R_{NL}^P , red line) configuration. (b) Net symmetric Hanle precession signal extracted from the two curves in (a) by taking $\Delta R_{NL} = (R_{NL}^P - R_{NL}^{AP})/2$. Here, no evidence of spin lifetime anisotropy is observed. In a TMDC/graphene system, the spin lifetime anisotropy stems from the valley-Zeeman interaction resulting from the TMD layer. However, unlike the existence of valleys in TMDC crystals, the Cu oxide is deposited by thermal evaporation in an amorphous state. In this regard, no spin lifetime anisotropy was expected in this system.

SUPPORTING REFERENCES

- (1) Stoner, E. C.; Wohlfarth, E. P. A Mechanism of Magnetic Hysteresis in Heterogeneous Alloys. *Philos. Trans. R. Soc. London. Ser. A, Math. Phys. Sci.* **1948**, *240* (826), 599–642.
- (2) Inglá-Aynés, J.; Guimarães, M. H. D.; Meijerink, R. J.; Zomer, P. J.; Van Wees, B. J. 24-Mm Spin Relaxation Length in Boron Nitride Encapsulated Bilayer Graphene. *Phys. Rev. B* **2015**, *92* (20), 201410.
- (3) D'Amico, I.; Vignale, G. Theory of Spin Coulomb Drag in Spin-Polarized Transport. *Phys. Rev. B - Condens. Matter Mater. Phys.* **2000**, *62* (8), 4853–4857.
- (4) Bandurin, D. A.; Torre, I.; Kumar, R. K.; Ben Shalom, M.; Tomadin, A.; Principi, A.; Auton, G. H.; Khestanova, E.; Novoselov, K. S.; Grigorieva, I. V.; Ponomarenko, L. A.; Geim, A. K.; Polini, M. Negative Local Resistance Caused by Viscous Electron Backflow in Graphene. *Science (80-.)* **2016**, *351* (6277), 1055–1058.
- (5) Vasquez, R. P. Cu₂O by XPS. *Surf. Sci. Spectra* **1998**, *5* (4), 257–261.
- (6) Alexander V. Naumkin; Kraut-Vass, A.; Gaarenstroom, S. W.; Powell, C. J. NIST Standard Reference Database 20. **2012**.
- (7) Seah, M. P.; Dench, W. A. Quantitative Electron Spectroscopy of Surfaces: A Standard Data Base for Electron Inelastic Mean Free Paths in Solids. *Surf. Interface Anal.* **1979**, *1* (1), 2–11.
- (8) Biesinger, M. C. Advanced Analysis of Copper X-Ray Photoelectron Spectra. *Surf. Interface Anal.* **2017**, *49* (13), 1325–1334.
- (9) Inglá-Aynés, J.; Groen, I.; Herling, F.; Ontoso, N.; Safeer, C. K.; De Juan, F.; Hueso, L. E.; Gobbi, M.; Casanova, F. Omnidirectional Spin-to-Charge Conversion in Graphene/NbSe₂van Der Waals Heterostructures. *2D Mater.* **2022**, *9* (4), 045001.